Analysis And Modeling Of Piezoelectric Resonant Body Transistors

by

Radhika Marathe

Submitted to the
Department of Electrical Engineering and Computer Science
in Partial Fulfillment of the Requirements for the Degree of

Master of Science in Electrical Engineering and Computer Science

at the

Massachusetts Institute of Technology

June 2011

Signature of Author.....
Department of Electrical Engineering and Computer Science
May 20, 2011

Certified by.....
Dana Weinstein
Assistant Professor of Electrical Engineering and Computer Science
Thesis Supervisor

Accepted by .....
Professor Leslie A. Kolodziejski,
Chair, Department Committee on Graduate Students
Professor of Electrical Engineering

Abstract

Microelectromechanical resonators are advantageous over traditional LC tanks in transceiver circuits due to their high quality factors (Q > 10000), small size and low power consumption. These characteristics enable monolithic integration of MEMS–based resonators as high-performance filters and oscillators at GHz frequencies in wireless communication technology. Similarly, they are desirable as high-precision low phase-noise clocking sources in microprocessor technology. To this end, both dielectric and piezoelectric transduction based resonators have been demonstrated as viable alternatives to their electrical counterparts. Dielectric (or electrostatic) based resonators take advantage of the cost-scaling of Silicon micromachining and the excellent mechanical properties of single crystal Silicon, leading to high-Q low cost resonators that have been extensively explored over the past two decades. However, piezoelectric based resonators have generally been preferred over these due to their high electromechanical coupling coefficients ($k_T^2 \sim 4\%$) resulting in a much lower insertion loss, larger power handling defined by the breakdown voltage across piezoelectric films and ease of packing and integration into transceiver circuitry.

Transistor sensing has been employed in both electrostatic and piezoelectric devices to enhance sensing efficiency. In particular, the Resonant Body Transistor (RBT) has been demonstrated as an electrostatic device which utilizes internal dielectric transduction to achieve the highest frequency acoustic resonators to date. The FET based sensing also pushes the operating frequency higher fundamentally as it is now limited only by the transistor cutoff frequency. In this work, we investigate the RBT geometry with piezoelectric transduction for more efficient and low loss drive and sense. To this end a full analytical model of the Piezoelectric RBT is presented explaining the piezoelectric drive and piezoelectric-piezoresistive mechanism-based sensing. The equivalent circuit model is presented and optimized for linearity in the AC output current to minimize harmonic distortion and for lowering the motional impedance . It is finally compared to a traditional piezoelectric resonator while discussing the tradeoffs with respect to the desired applications.

ACKNOWLEDGEMENTS

I would like to extend my heartfelt gratitude to my research advisor, Professor Dana Weinstein, who has been a constant source of innovation and motivation over the past two years. She has not only mentored this particular project with her ideas, attention to detail and thought-provoking questions but has inspired me on much broader level, by providing an excellent example of her technical, management and networking skills. I am also thankful to my colleagues Wentao Wang and Laura Popa for their optimism and support throughout the project and for sharing my joys and sorrows in the cleanroom.

This work was carried out in part through the use of MIT's Microsystems Technology Laboratories. I sincerely thank all the members of MTL staff for providing excellent training, and sometimes re-training, on each of the tools used for this process. I would like to especially thank Vicky Diadiuk, Paul Tierney, Eric Lim, Kristofor Payer and Dennis Ward for their feedback and discussions that leading to process improvements. I am also grateful to the entire MTL Computation Team for maintaining MTL's CAD facilities and for restoring my data after my inadvertent but frequent software crashes.

Finally, I would like to extend my gratitude to all my friends, who have always encouraged and supported me through my evolving interests and career paths, and my family, for all their love and entirely biased but unconditional belief in my abilities.

INDEX

LIST OF FIGURES

LIST OF TABLES

BACKGROUND

1.1 Introduction to MEMS Resonators

Microelectromechanical resonators have a promising future in communications and microprocessor technology due to their performance advantages over existing counterparts. A portion of communication devices today use traditional LC tanks to provide filters or frequency sources which have difficulty meeting the insertion loss, quality factor and out-of-band rejection for the filtering standards today. These issues are effectively addressed by microelectromechanical resonators, which, with quality factors (Q) that are often a few orders of magnitude higher than LC circuits, enable multi-frequency, multi-band filters and oscillators in wireless communication technology.

Currently, a larger proportion of cell phones use large passive mechanical components such as Surface Acoustic Wave (SAW) and Film Bulk Acoustic Resonator (FBAR) based technology which have seen very little miniaturization over the past few years and cannot be integrated into Silicon technology. For these, microelectromechanical resonators provide a low small size, integrable, low cost and low-power alternative which makes them attractive candidates which can keep pace with the miniaturization and integration trends of the wireless communication industry. This leads to the about the vision of a single integrated solution for radio components including RF and IF filters, mixers and oscillators onto a single chip as shown in Figure [1.1].

Similarly, in microprocessor technology, small-size Silicon-based electromechanical resonators can provide synchronized low power clocking arrays with reduced jitter and skew, allowing the technology to scale to high frequencies with high-precision clocking.

1.2 Types of MEMS Resonators

Since the demonstration of the first resonant structure in the form of the Resonant Gate Transistor by Nathanson in 1967 [1] MEMS-based resonating structures have been designed in a variety of shapes and

forms. They operate in various resonant eigenmodes, including flexural, contour and longitudinal, and they may be actuated and sensed (i.e. transduced) in a variety of ways, some of the most prevalent ones

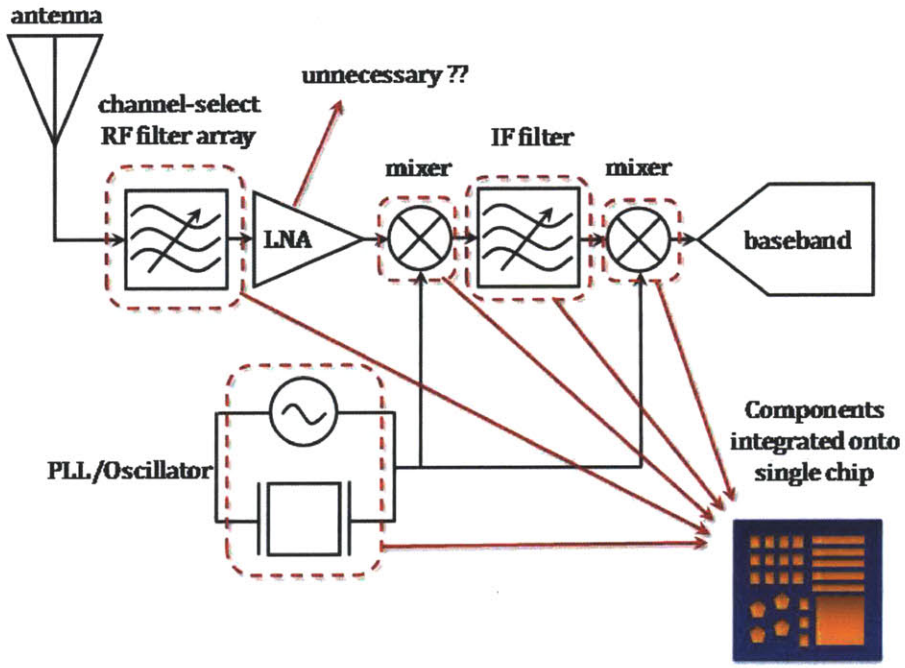

Figure 1.1: Vision for a single integrated solution for radio components employing multi-band filters, mixers and oscillators onto a single chip.

being capacitive, piezoelectric, thermal and optomechanical. This project pertains to longitudinal mode bulk acoustic wave resonators, so we will first go into the details of this particular mode. Similarly, from a transduction perspective, we will discuss the capacitive or dielectric based and piezoelectric mechanisms as they are most relevant to this project.

1.3 Mechanics of Vibration

We discuss the mechanics of the longitudinal bulk mode of vibrations of bars in order to better understand the resonant eigenmode of the device under consideration and set up the wave equation for the same.

Assuming we have a device with a resonant length L, operating in the nth mode of resonance given by frequency f_n which corresponds to the angular frequency ω_n. The wavelength λ_n for the nth mode is give by:

$$\lambda_n = \frac{n}{2\,L}$$

and thus the wave number k_n is given by

$$k_n = \frac{2\,\pi}{\lambda_n} = \frac{n\,\pi}{L}$$

The acoustic velocity, vel, in this device is given by

$$vel = \sqrt{\frac{E_{eff}}{\rho_{eff}}}$$

where E_{eff} and ρ_{eff} are the effective Young's modulus and the density of the device.

Using these, we have the resonant frequency given by:

$$\omega_n = 2\pi f_n = 2\,\pi\,\frac{vel}{\lambda_n} = 2\,\pi\frac{n}{2\,L}\sqrt{\frac{E_{eff}}{\rho_{eff}}} = \frac{n\,\pi}{L}\sqrt{\frac{E_{eff}}{\rho_{eff}}}$$

Using the above equations, we can now construct the wave equation for the modal shape for this device, modeling it as a lateral mode bar resonator:

$$u(x,t) = \mathrm{U_0}\sin(k_n x)\cdot e^{j\omega_n t}$$

Once the wave equation is set up, we may solve for the amplitude of vibrations using the equation for damped longitudinal vibrations in a bar. For a bar with cross sectional area A, and a driving stress function σ, this equation is given by:

$$\mathrm{A}\rho_{eff}\frac{\partial^2 u(x,t)}{\partial t^2} - \mathrm{Ab}\frac{\partial^3 u(x,t)}{\partial t\partial x^2} - \mathrm{AE}_{eff}\frac{\partial^2 u(x,t)}{\partial x^2} = \mathrm{A}\frac{\mathrm{d}\sigma_{\mathrm{drive}}}{\mathrm{dx}}$$

However, before we can use this equation to calculate the amplitude of vibrations, we need to calculate the damping coefficient b in terms of material properties and other measurable quantities.

We start by cancelling the term A throughout and substituting $u(x,t) = \mathrm{U(t)sin}(k_n x)$ into the beam equation, where $\mathrm{U(t)} = \mathrm{U}_0 e^{j\omega_n t}$. Thus we get:

$$\rho_{eff}\frac{\partial^2 \mathrm{U(t)sin}(k_n x)}{\partial t^2} + {k_n}^2\frac{\partial\, \mathrm{U(t)sin}(k_n x)}{\partial t} + \mathrm{E}_{eff}{k_n}^2\,\mathrm{U(t)sin}(k_n x) = \frac{\mathrm{d}\sigma_{\mathrm{drive}}}{\mathrm{dx}} = \mathrm{f(x,t)}$$

We take the Laplace transform on both sides with respect to the variable t and set initial conditions of displacement and strain to zero. Let the Laplace transform of $\mathrm{U(t)sin}(k_n x)$ be denoted by $\mathfrak{U}(x,s)$ and the Laplace transform of the RHS be denoted by $F(x,s)$ to get:

$$\mathfrak{U}(\mathrm{x,s})[\rho_{eff}\, s^2 + \mathrm{b}{k_n}^2 s + \mathrm{E}_{eff}{k_n}^2] = F(x,s)$$

This may be re-written as the transfer function H(s) given by:

$$\mathrm{H(s)} = \frac{\mathfrak{U}(\mathrm{x,s})}{F(x,s)} = \frac{\dfrac{1}{\rho_{eff}}}{s^2 + \dfrac{\mathrm{b}{k_n}^2}{\rho_{eff}}s + \dfrac{\mathrm{E}_{eff}\,{k_n}^2}{\rho_{eff}}}$$

This is a second order system response, the denominator of which may be compared to the denominator of the second order harmonic oscillator response with Quality factor (Q) and an undamped resonant frequency, ω_n, which is given by:

$$\mathrm{H(s)} = \frac{{\omega_n}^2}{s^2 + \dfrac{\omega_n}{\mathrm{Q}}s + {\omega_n}^2}$$

Equating the constant, we see that

$$\frac{\mathrm{E}_{eff}\,{k_n}^2}{\rho_{eff}} = {\omega_n}^2$$

which is consistent with our equations and so we may equate the coefficient of the s term to get the damping coefficient b as:

$$\frac{\mathrm{b}{k_n}^2}{\rho_{eff}} = \frac{\omega_n}{\mathrm{Q}} = \frac{k_n}{Q}\sqrt{\frac{E_{eff}}{\rho_{eff}}}$$

$$b = \frac{\sqrt{\mathrm{E}_{eff}\rho_{eff}}}{k_n \mathrm{Q}}$$

1.4 Transduction Mechanisms

1.4.1 Dielectric or Capacitive Transduction

After a mechanical analysis of the resonator as a longitudinal mode bar resonator, we turn our attention towards driving and sensing this resonant mode.

One of the pioneering capacitive structures is the comb-drive resonator demonstrated by Tang et. al. in 1989 [2]. This comb drive resonator consisted of a large suspended structure with interdigitated fingers on its sides which would form capacitors with its surrounding anchored comb structure as shown in Figure[1.2 (a)].

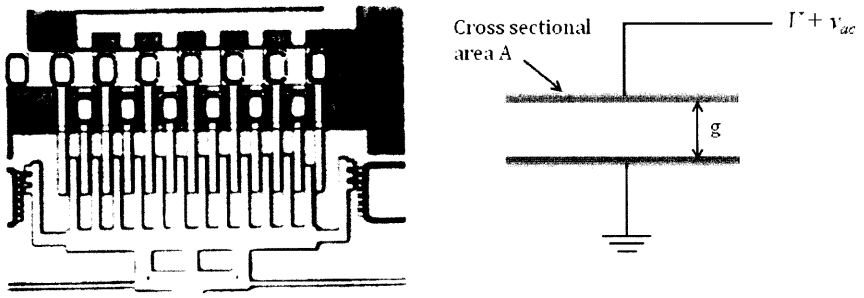

Figure 1.2: (a) Optical Micrograph of Comb drive [3] showing interdigitated fingers, (b) schematic of single capacitor driven with a DC bias V with small AC driving voltage v_{ac}

The air gap capacitors thus formed could be used to actuate the resonance of this proof mass suspended on beams using the capacitive force. Mathematically, for a capacitor structure in Figure [1.2 (b)] the capacitance C is given by:

$$C = \frac{\varepsilon_0 A}{g}$$

For a DC bias voltage $V+$ a small AC bias $v_{ac}e^{j\omega t}$ applied across the plates, the energy E and the capacitive force F are given by:

$$E = \frac{1}{2} C (V + v_{ac}e^{j\omega t})^2$$

$$F = \frac{\partial E}{\partial u}$$

$$= \frac{\partial}{\partial u}\frac{1}{2}\frac{\varepsilon_0 A}{g+u}(V + v_{ac}e^{j\omega t})^2$$

$$= \frac{1}{2}(V^2 + 2Vv_{ac}e^{j\omega t} + v_{ac}^2 e^{j2\omega t})\frac{\partial}{\partial u}\frac{\varepsilon_0 A}{g+u}$$

$$= \frac{-1}{2}(V^2 + 2Vv_{ac}e^{j\omega t} + v_{ac}^2 e^{j2\omega t})\frac{\varepsilon_0 A}{(g+u)^2}$$

We assume the displacement of the capacitor plates due to this force, x, is much smaller than the initial distance between the plates, g. We also see that the voltage term in the brackets has a DC component and AC components at ω and 2ω. Taking only the AC component at ω into account, the force is given by:

$$\approx \frac{\varepsilon_0 A}{g^2} V v_{ac} e^{j\omega t}$$

As discussed previously in Section [1.3], the displacement wave form for this resonator is given by:

$$u(x,t) = \mathrm{U}_0 \sin(k_n x) \cdot e^{j\omega_n t}$$

On the sensing side, we apply a DC bias voltage V on the capacitor plates to get an AC output current

$$i_{out} = \frac{\partial Q}{\partial t} = V\frac{\partial C}{\partial t}$$

$$= V\varepsilon_0 A \frac{\partial}{\partial t}\frac{1}{g+u}$$

Again assuming that the displacement, $u \ll g$,

$$i_{out} = -\frac{V\varepsilon_0 A}{g^2}\frac{\partial u}{\partial t}$$

$$= -j\omega_n \frac{V\varepsilon_0 A}{g^2}\mathrm{U(x)} \cdot e^{j\omega_n t}$$

where U(x) is the amplitude term dependent on the x coordinate of the capacitor plate with respect to the coordinate system.

Based on the above, one of the first improvements in capacitively transduced resonators came in the form of substituting a high-k dielectric film in place of the air gap in this capacitor [4], which boosted the force term as well as the output current term by the magnitude of the relative permittivity of the dielectric. This dramatically improved the transduction efficiency and reduced the motional impedance (R_x) values of

capacitive resonators by reducing the gap size. The next improvement came in terms of integrating the dielectric films inside the body of the resonator [5] which avoided the losses from acoustic energy leaking into the surrounding material through the dielectric films and allowed the more efficient mechanism of piezoresistive sensing to be employed in place of capacitive sensing, thus lowering the motional impedance further. Finally, the Resonant Body Transistor [6] or RBT shown in Figure [1.3], used these integrated dielectric films to create a transistor based resonators with high-k gate dielectrics for actuation and sensing which not only allowed for further reduced R_x values but also showed promise for resonator frequency scaling with transistor technology.

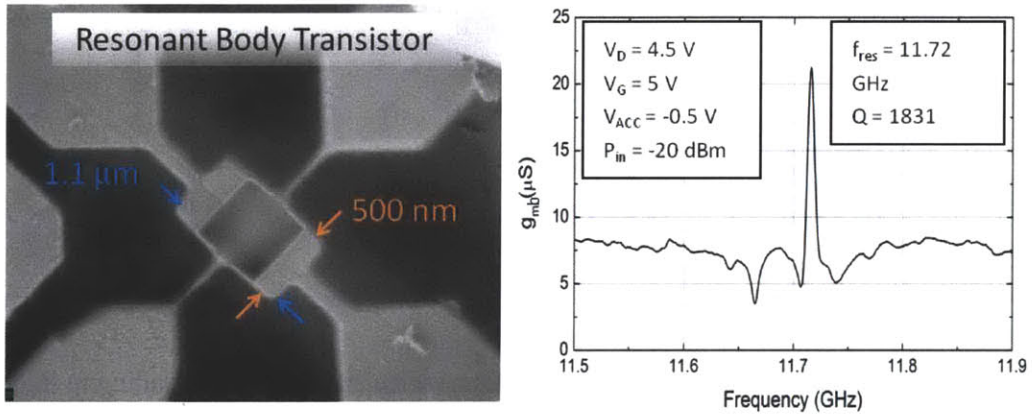

Figure 1.3: (left) An image of the Resonant Body Transistor (right) along with its frequency response.

1.4.2 Piezoelectric Transduction

Piezoelectric transduction is one of the most efficient transduction mechanisms used in MEMS based resonators. The underlying principle used is the piezoelectric property of materials such as AlN. These materials develop a strain in their bulk in response to an applied electric field applied across them and vice-versa, electric charge is induced on the surface of these materials in response to a mechanical strain. The fundamental equations of piezoelectricity may be expressed in the following manner:

$$T = cS - e^T E$$

$$D = eS + \varepsilon E$$

in which S is the strain matrix, T is the stress, c is the compliance matrix. E is the electric field applied externally and D is the electric displacement matrix. e and e^T are the piezoelectric matrices (direct and transpose) and ε is the dielectric matrix [7].

For a crystal with hexagonal symmetry such as AlN, this matrix assumes the following form: [8]

$$\begin{bmatrix} T_1 \\ T_2 \\ T_3 \\ T_4 \\ T_5 \\ T_6 \end{bmatrix} = \begin{bmatrix} c_{11} & c_{12} & c_{13} & 0 & 0 & 0 \\ & c_{11} & c_{12} & 0 & 0 & 0 \\ & & c_{33} & 0 & 0 & 0 \\ & & & c_{44} & 0 & 0 \\ & & & & c_{44} & 0 \\ & & & & & \frac{c_{11}-c_{12}}{2} \end{bmatrix} \begin{bmatrix} S_1 \\ S_2 \\ S_3 \\ S_4 \\ S_5 \\ S_6 \end{bmatrix} - \begin{bmatrix} 0 & 0 & e_{31} \\ 0 & 0 & e_{31} \\ 0 & 0 & e_{33} \\ 0 & e_{24} & 0 \\ e_{15} & 0 & 0 \\ 0 & 0 & 0 \end{bmatrix} \begin{bmatrix} E_1 \\ E_2 \\ E_3 \end{bmatrix}$$

$$\begin{bmatrix} D_1 \\ D_2 \\ D_3 \end{bmatrix} = \begin{bmatrix} \varepsilon_1 & 0 & 0 \\ & \varepsilon_1 & 0 \\ & & \varepsilon_3 \end{bmatrix} \begin{bmatrix} E_1 \\ E_2 \\ E_3 \end{bmatrix} + \begin{bmatrix} 0 & 0 & 0 & 0 & e_{15} & 0 \\ 0 & 0 & 0 & e_{15} & 0 & 0 \\ e_{31} & e_{31} & e_{33} & 0 & 0 & 0 \end{bmatrix} \begin{bmatrix} S_1 \\ S_2 \\ S_3 \\ S_4 \\ S_5 \\ S_6 \end{bmatrix}$$

Piezoelectric coupling coefficients are much stronger than dielectric coefficients leading to R_x values of a few tens of Ωs vs the kΩ range values obtained for dielectric based resonators as shown in Figure [1.4]. The tradeoff is often the lowering of the quality factor (Q) which is intrinsically lower for the electrode material such as Molybdenum surrounding the piezoelectric materials [9] which form the bulk of these resonators. An effective solution was shown by Abdolvand et al [10] in terms of boosting both the power-handling and Q values of piezoelectric resonators by mounting them on a silicon substrate, with an inherently higher material limit on the quality factor. Techniques combining dielectric and piezoelectric sensing [11] have also addressed this issue but ultimately, the difficulty in integrating piezoelectric materials with silicon-based circuitry presents an inherent problem in scaling these devices to higher frequencies with transistor technology.

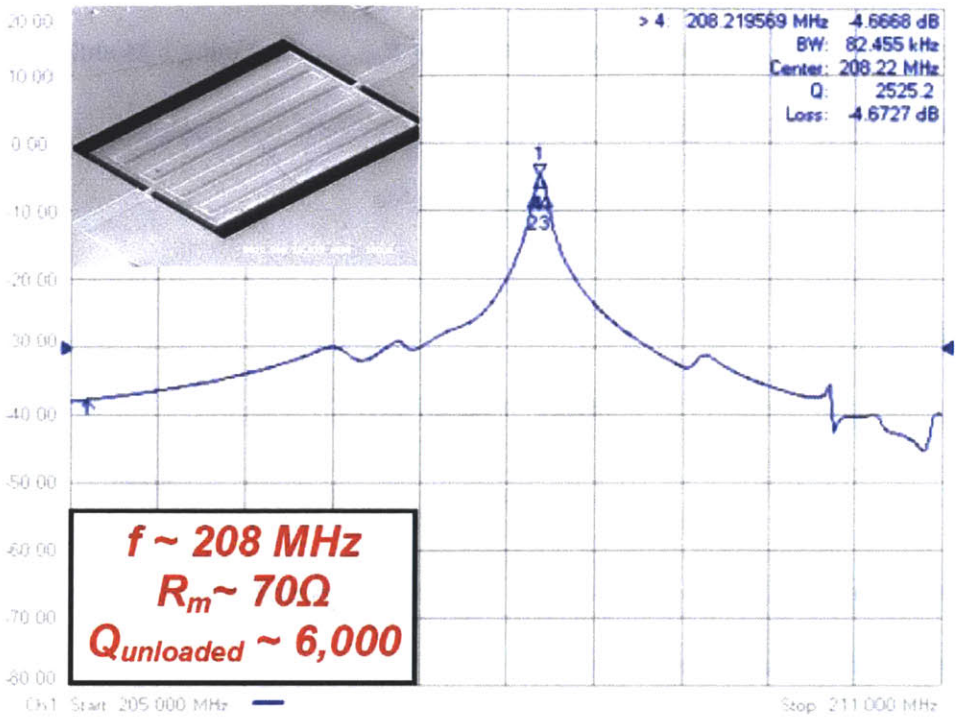

Figure 1.4: Frequency response (S_{21}) of a Piezoelecric Resonator mounted on Silicon showing SEM of device used (inset) [10]

1.5 Electrostriction

Electrostriction is a property of insulators associated with randomly oriented domains within the material. In the presence of an electric field, these domains form localized polarizations which can attract each other, causing a strain to form in the material. Mathematically, electrostriction is defined as the quadratic coupling between strain (s) and electric field (E), or between strain and polarization (P). This is a fourth-rank tensor expressed by the following relationships

$$s_{ij} = c^E{}_{ijkl} T_{ij} + M_{ijmn} E_m E_n$$

$$s_{ij} = c^P{}_{ijkl} T_{ij} + Q_{ijmn} P_m P_n$$

Using the second equation above, we see that for a piezoelectric film such as AlN, the strain along the direction i, j is defined as s_{ij}, is related to the Stress along that direction T_{ij}, through the compliance $c^P{}_{ijkl}$ and to the polarization along the directions m and n, through the coefficient Q_{ijmn} . If we apply an

electric field in only one direction, say the c-axis of the piezoelectric material, the resultant electrostrictive stress, σ_{estric}, will be expressed in terms of E_{piezo} , the Young's Modulus of the material and s_{33}, the strain along the c-axis as:

$$\sigma_{estric} = E_{piezo}\, s_{33}$$

This expands to:

$$\sigma_{estric} = E_{piezo}\, Q_{33} {P_3}^2$$

$$= E_{piezo}\, Q_{33} \varepsilon_0^2 \left(k_{piezo} - 1\right)^2 \left(\frac{V}{g}\right)^2$$

Where ε_0 is the permittivity of free space, k_{piezo}, is the relative permittivity of the piezoelectric film of thickness g, and V is the voltage applied across it.

Electrostriction is usually a secondary mechanism used for actuating a MEMS resonator.

Keeping these mechanisms in mind, we now introduce the Piezoelectric Resonant Body Transistor proposed in this work.

THE PIEZOELECTRIC RESONANT BODY TRANSISTOR

2.1 Motivation

As transistor technology continues scaling to the deep submicron range driven by Moore's Law, transistor threshold frequencies have increased, enabling transceiver circuitry to be designed in the tens of GHz range. The released and unreleased resonant body transistors [6, 12] have been demonstrated as dielectric based, high Q components with high spectral purity that utilize the inherent gain of the field effect transistor for amplifying the mechanical resonance signal. However, the impedance of these devices is still orders of magnitude greater than those of piezoelectric devices. At the same time, devices using piezoelectric transduction [13, 14] have been demonstrated in the multi-GHz range with low impedance values due to the high coupling coefficients of piezoelectric materials. Combining the amplifying effects of FET sensing with the high transduction efficiency of piezoelectric materials suggests the design of the Piezoelectric Resonant Body Transistor.

2.2 Principle of Operation

It is useful to discuss the basics of the Resonant Body Transistor (RBT) as a starting point for the Piezoelectric RBT as they share some common features. From the electrical point of view, the RBT is a two-gate transistor, with a dielectric such as Silicon Nitride or Hafnia in place of the gate oxide. The transistor is biased into saturation by tying the source to ground and applying a DC bias to the sensing gate and the drain. The back gate is also the actuation gate which is biased into accumulation. From a mechanical point of view, the RBT is a longitudinal mode bar resonator which is driven capacitively by applying a small AC bias to the back gate or actuation gate to launch acoustic waves into the device. The device resonates perpendicular to the direction of the channel. The resonance is sensed piezoresistively with a small capacitive contribution at the channel which is observed as a modulation in the transconductance.

The Piezoelectric RBT uses piezoelectric films in place of the gate oxide of the Dielectric RBT [Figure 2.1]. On the driving side, acoustic vibrations are now driven piezoelectrically, through the e33 coupling coefficient resulting in a higher driving stress and larger amplitude of vibrations. On the sensing side, the piezoelectric film experiences strain due to the longitudinal vibrations in the bar at resonance, and this results in a modulation in the polarization and hence electric field across the film through the inverse piezoelectric coefficient. This is modeled as a modulation in net gate voltage and is usually the dominant term over piezoresistive and capacitive contribution. The full analytical model for the device is discussed below.

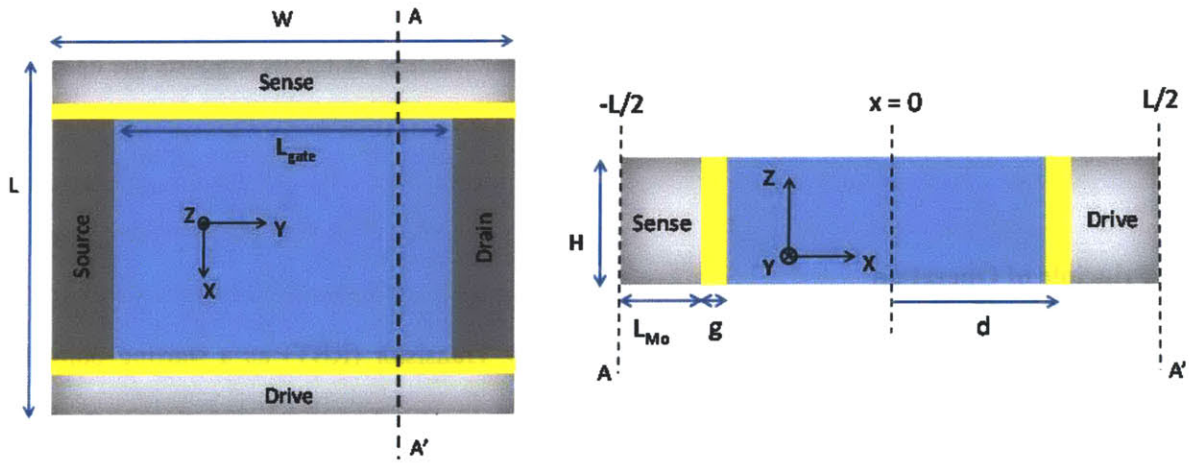

Figure 2.1: (*a*) Schematic of piezoelectrically transduced Resonant Body transistor. AlN piezoelectric films are used in place of the gate oxide for a double-gate transistor for sensing and actuation. (*b*) Cross section along A-A' line.

2.1 Table of Parameters

Parameter	Description
L	Length of Device along resonant dimension
W	Width of device, along direction of channel
H	Thickness of device, determined by thickness of device layer on SOI wafer
V_D	Drain Voltage
V_A	Back-gate DC voltage
v_{ac}	Back-gate AC voltage
g	Thickness of Piezoelectric film
e_{33}	Piezoelectric coefficient along c-axis
Q_{33}	Electrostrictive Coefficient of piezoelectric
n	Number of harmonic
f_n	Frequency of operation at nth harmonic
U_0	Amplitude of vibrations
d	Center-to-center distance between piezoelectric films
E_x	Young's modulus of material x along resonant dimension
ρ_x	Density of material x
L_{Mo}	Length of Mo electrode along resonant dimension
Q	Quality factor of device at frequency f
ε_0	Permittivity of free space
k_{piezo}	Relative permittivity of piezoelectric material
L_{gate}	Length of gate
μ_n	Electron mobility in channel
V_T	Threshold Voltage
k_{Si}	Relative Permittivity of Si
q	Elementary Charge
N_A	Doping of the device body
k	Boltzmann Constant
T	Temperature of operation
n_i	Intrinsic Carrier Concentration in Si
Q_{piezo}	Induced sheet charge in channel due to piezoelectric effect
V_{piezo}	Induced voltage on gate due to piezoelectric effect
π_{111}	Piezoresistive coefficient in Si along the <111> direction

2.3 Driving of Acoustic Vibrations

2.3.1 Piezoelectric Contribution

The device is operated as a transistor by biasing the source at ground and applying a DC voltage V_D to the drain and a DC voltage V_G to the sensing gate. The back gate or driving gate of the piezoelectric RBT is biased into accumulation by applying a DC voltage V_A. We then apply a small AC voltage $v_{ac}e^{j\omega_n t}$ to the drive gate, in addition to V_A, to launch acoustic waves into the device. Thus, the net voltage applied across the back gate is $V_A + v_{ac}e^{j\omega_n t}$ on the source side and $V_A + v_{ac}e^{j\omega_n t} - V_D$ on the drain side. This results in an average driving voltage of

$$\frac{V_A + v_{ac}e^{j\omega_n t} - V_D}{2}$$

and an average value for the electric field across the piezoelectric film of thickness g is

$$\frac{V_A + v_{ac}e^{j\omega_n t} - V_D}{2\,g}$$

Using the Piezoelectric equations discussed previously, the resultant in-plane stress in the piezoelectric film, σ_{piezo}, along the direction of the Electric field, which is also along the direction of the c-axis given by

$$\sigma_{piezo} = e_{33}\frac{V_A + v_{ac}e^{j\omega_n t} - V_D}{2\,g} = e_{33}\left(\frac{V_A - V_D}{2\,g} + \frac{v_{ac}e^{j\omega_n t}}{2\,g}\right)$$

Hence the AC stress, σ_p, relevant for the amplitude of vibration calculation, is given by

$$\sigma_p = e_{33}\frac{v_{ac}e^{j\omega_n t}}{2\,g}$$

2.3.2 Electrostrictive Contribution

In addition to the piezoelectric effect, electrostriction also contributes to stress in the AlN. As discussed in section [1.5], the stress is induced due to electrostriction, σ_{estric}, given by:

$$\sigma_{estric} = E_{piezo}\,Q_{33}\varepsilon_0^2\,(k_{piezo} - 1)^2\left(\frac{V_A - V_D + v_{ac}e^{j\omega_n t}}{2\,g}\right)^2$$

$$= \frac{E_{piezo}\, Q_{33} \varepsilon_0^2 \left(k_{piezo}-1\right)^2}{4\, g^2} \left((V_A - V_D)^2 + 2(V_A - V_D) v_{ac} e^{j\omega_n t} + v_{ac}^2 e^{2j\omega_n t}\right)$$

Ignoring the DC component and the component at frequency $2\omega_n$, we have the AC component of the electrostrictive stress given by:

$$\sigma_e \approx \frac{E_{piezo}\, Q_{33} \varepsilon_0^2 \left(k_{piezo} - 1\right)^2}{2\, g^2} (V_A - V_D) v_{ac} e^{j\omega_n t}$$

Thus, the total driving stress will be $\sigma_{drive} = \sigma_p + \sigma_e$

2.4 Analyzing the waveform

2.4.1 The Resonant frequency

As discussed in section [1.3], we can now construct the wave equation for the modal shape for this device, modeling it as a lateral mode bar resonator:

$$u(x,t) = U_0 \sin(k_n x) \cdot e^{j\omega_n t}$$

where U_0 is the amplitude of vibrations and the wave number, k_n, for the n^{th} harmonic is given by

$$k_n = \frac{2\pi}{\lambda_n} = \frac{n\pi}{L}$$

and the resonant frequency, ω_n, given by:

$$\omega_n = \frac{n\pi}{L} \sqrt{\frac{E_{eff}}{\rho_{eff}}}$$

where E_{eff} and ρ_{eff} are the effective Young's modulus and the density of the device. In this case however, it is more straightforward to calculate the frequency using the method of fractional wavelengths than through the calculation of the above. For this, we note that at resonance, for a standing wave to be formed in the resonator, we have

$$L = n \frac{\lambda_n}{2}$$

As the resonator is made up for a stack of materials with different acoustic velocities, for a resonant frequency f_n the acoustic wavelength corresponding to a material is given by

$$\lambda_x = \frac{vel_x}{f_n}$$

Thus in the Moly electrodes, this wavelength would be given by:

$$\lambda_{Mo} = \frac{vel_{Mo}}{f_n} = \frac{1}{f_n}\sqrt{\frac{E_{Mo}}{\rho_{Mo}}}$$

Similarly , we may determine the acoustic wavelengths in each of the films using the Young's moduli, E, of and density, ρ, of the constituent materials, Si for Silicon, $piezo$ for the piezoelectric film and Mo for the Molybdenum electrodes. Now due to condition of forming a standing wave at resonance, we require that the total length is a multiple of a half-wavelength. Since the wavelength in each material is different, we may say instead that the sum of fractional wavelengths in each material constituting the resonator has to be a multiple of ½. This may be expressed as:

$$\frac{2\,L_{Mo}}{\lambda_{Mo}} + \frac{2\,L_{piezo}}{\lambda_{piezo}} + \frac{L_{Si}}{\lambda_{Si}} = \frac{n}{2}$$

Substituting for the expression for the wavelengths, we have

$$f_n \left(\frac{2\,L_{Mo}}{\sqrt{\frac{E_{Mo}}{\rho_{Mo}}}} + \frac{2\,L_{piezo}}{\sqrt{\frac{E_{piezo}}{\rho_{piezo}}}} + \frac{L_{Si}}{\sqrt{\frac{E_{Si}}{\rho_{Si}}}} \right) = \frac{n}{2}$$

$$f_n = \left(\frac{n}{2}\right) \frac{1}{\frac{2\,L_{Mo}}{\sqrt{\frac{E_{Mo}}{\rho_{Mo}}}} + \frac{2\,L_{piezo}}{\sqrt{\frac{E_{piezo}}{\rho_{piezo}}}} + \frac{L_{Si}}{\sqrt{\frac{E_{Si}}{\rho_{Si}}}}}$$

2.4.2 E_{eff} and ρ_{eff}

We now calculate E_{eff} and ρ_{eff}, the effective Young's modulus and the density of the device. To find the values of these constants, we first observe that the vibrations happen along X axis, which consists of a 5-film stack [Figure 2.1b]. These five films may be considered to be five springs vibrating in series in

response to a bulk acoustic wave. We can assume each of these films to be a cuboidal bar and calculate the spring constant for the same. For such a bar with length l, and cross sectional area $w\ X\ h$, the spring constant k_{bar} for a force along the length l, is given by:

$$k_{bar} = \frac{E\ w\ h}{l}$$

Thus, in this case, for the Moly film, with Young;s modulus E_{Mo}, the spring constant k_{Mo} will be

$$k_{Mo} = \frac{E_{Mo}\ W\ H}{L_{Mo}}$$

Similarly, we write the spring constant for the other films as well. We also write the effective spring constant, k_{eff}, using the effective resonant length of the device, which is just L as

$$k_{eff} = \frac{E_{eff}\ W\ H}{L}$$

For these five springs vibrating in series, we now relate the individual spring constants to the effective spring constant as:

$$\frac{1}{k_{eff}} = \sum \frac{1}{k_i}$$

$$\frac{L}{E_{eff}\ W\ H} = \frac{2\ L_{Mo}}{E_{Mo}\ W\ H} + \frac{2\ L_{piezo}}{E_{piezo}\ W\ H} + \frac{L_{Si}}{E_{Si}\ W\ H}$$

Canceling the common terms and rearranging we get,

$$E_{eff} = \frac{L}{\frac{2\ L_{Mo}}{E_{Mo}} + \frac{2\ L_{piezo}}{E_{piezo}} + \frac{L_{Si}}{E_{Si}}}$$

Using the above value, we now calculate the effective density using the relation

$$f_n = \frac{\omega_n}{2\ \pi} = \frac{n\ \pi}{2\ \pi\ L}\sqrt{\frac{E_{eff}}{\rho_{eff}}}$$

$$\rho_{eff} = \left(\frac{n}{2\ f_n\ L}\right)^2 E_{eff}$$

2.4.3 Amplitude of Vibrations

We use the equation for damped vibrations in a bar (1D) to solve for the amplitude of vibrations:

$$A\rho_{eff}\frac{\partial^2 u(x,t)}{\partial t^2} - Ab\frac{\partial^3 u(x,t)}{\partial t \partial x^2} - AE_{eff}\frac{\partial^2 u(x,t)}{\partial x^2} = A\frac{d\sigma_{drive}}{dx}$$

where the damping coefficient, b, is as calculated in Section [1.3] to be:

$$b = \frac{\sqrt{E_{eff}\rho_{eff}}}{k_n Q}$$

Canceling the cross section area term A, substituting $u(x,t) = U_0 \sin(k_n x)\cdot e^{j\omega_n t}$ and $\sigma_{drive} = \sigma_p$ into the above we have,

$$-\rho_{eff}\omega_n{}^2 e^{j\omega_n t} U_0 \sin(k_n x) + jb\omega_n e^{j\omega_n t} k_n{}^2 U_0 \sin(k_n x) + E_{eff} e^{j\omega_n t} k_n{}^2 U_0 \sin(k_n x) = \frac{d\sigma_p}{dx}$$

which may be rewritten as

$$U_0 \sin(k_n x) = \frac{\frac{d\sigma_{drive}}{dx}}{(-\rho_{eff}\omega_n{}^2 e^{j\omega_n t} + jb\omega_n e^{j\omega_n t} k_n{}^2 + E_{eff} e^{j\omega_n t} k_n{}^2)}$$

The driving stress due to the piezoelectric film is a constant value through the thickness of the piezoelectric film, g, and zero elsewhere. Thus, the slope of the driving stress [15], may be represented as delta functions at interfaces of the piezoelectric film which is sandwiched between the Silicon body and the Moly back gate. As per our x-axis convention given in Figure [2.1] is the piezoelectric film extends from $x \in \left(d - \frac{g}{2}, d + \frac{g}{2}\right)$ on the drive side. Thus we have,

$$\frac{d\sigma_{drive}}{dx} = \sigma_{drive}\left[\delta\left(x - \left(d - \frac{g}{2}\right)\right) - \delta\left(x - \left(d + \frac{g}{2}\right)\right)\right]$$

Substituting this into the above equation, multiplying both sides by $\sin(k_n x)$ and integrating from -L/2 to L/2 gives us:

$$\int_{-L/2}^{L/2} U_0 \sin^2(k_n x)dx = \int_{-L/2}^{L/2} \frac{\sigma_p\left[\delta\left(x - \left(d - \frac{g}{2}\right)\right) - \delta\left(x - \left(d + \frac{g}{2}\right)\right)\right]\sin(k_n x)\,dx}{(-\rho_{eff}\omega_n{}^2 e^{j\omega_n t} + jb\omega_n e^{j\omega_n t} k_n{}^2 + E_{eff} e^{j\omega_n t} k_n{}^2)}$$

$$U_0 = \frac{2\sigma_{drive}}{L\, e^{j\omega_n t}\left(-\rho_{eff}\omega_n{}^2 + jb\omega_n k_n{}^2 + E_{eff}k_n{}^2\right)}\left(\sin\left(k_n d - \frac{k_n g}{2}\right) - \sin\left(k_n d + \frac{k_n g}{2}\right)\right)$$

Reducing the second bracket using the trigonometric identity

$$\sin A - \sin B = 2\sin\frac{(A-B)}{2}\cos\frac{(A+B)}{2}$$

we get,

$$\sin\left(k_n d - \frac{k_n g}{2}\right) - \sin\left(k_n d + \frac{k_n g}{2}\right) = -2\sin\left(\frac{k_n g}{2}\right)\cos(k_n d)$$

Thus, substituting this into U_0 we get,

$$U_0 = = \frac{2\sigma_{drive}}{L\, e^{j\omega_n t}\left(-\rho_{eff}\omega_n{}^2 + jb\omega_n k_n{}^2 + E_{eff}k_n{}^2\right)}\sin\left(\frac{k_n g}{2}\right)\cos(k_n d)$$

2.5 Sensing of Acoustic Vibrations

2.5.1 Assumptions for Sensing Side: [16]

1. The mobility in the channel is independent of electric field, velocity of electrons is directly proportional to E-field.
2. The gradual channel approximation holds - Gate field (perpendicular to the channel) is much greater than drift field (parallel to current flow).
3. Sheet Charge Approximation holds - All inversion electrons are assumed to be in a very thin layer at the AlN-Si interface as compared to the thickness of the bulk or the Piezoelectric film.
4. Semiconductor surface not biased into degeneracy.
5. All of the bulk is uniformly doped and fully depleted.
6. Diffusion currents are negligible with respect to drift currents.
7. Surface state charge per unit area is constant.
8. Generation and recombination currents are negligible.

9. Surface state charge is zero.
10. The channel is "long", no short channel effects are accounted for.
11. Sub-threshold current is negligible and the transistor is off at that point for all calculations.

2.5.2 Calculation of DC current

When all the above assumptions hold, the DC current in a field effect transistor whose source is tied to ground and the gate is biased at V_{GS} and drain is biased at V_{DS} , with a threshold voltage V_T, is given by two simple relations. In the linear regime, when $V_{DS} \leq V_{GS} - V_T$, we have the current I_{DCLin} given as

$$I_{DCLin} = \frac{H}{L_{gate}} \mu_n C_{piezo}(V_{GS} - V_T - \frac{V_{DS}}{2})V_{DS}$$

In the saturation regime we have $V_{DS} \geq V_G - V_T$, and the current I_{DCsat} is given by

$$I_{DCsat} = \frac{H}{2\,L_{gate}} \mu_n C_{piezo}(V_{GS} - V_T)^2$$

2.5.3 Calculation of Threshold Voltage [17]

a) For "long" bulk (i.e. maximum depletion region achieved)

In this case, the threshold Voltage, V_T,is calculated using the formula:

$$V_T = \phi_{ms} + \phi_{sth} + \frac{Q_{dmax}}{C_{piezo}}$$

where the difference in work functions ϕ_{ms} between the body and the electrode material, also known as the flatband voltage

$$\phi_{ms} = -\frac{W_{Si} - W_{Moly}}{q}$$

where the subthreshold voltage is given by $\phi_{sth}$where q is elementary charge, , k is the Boltzmann constant, T is the temperature, N_A is the doping of the bulk Silicon region and n_i is the intrinsic carrier density

$$\phi_{sth} = \frac{2\,k\,T}{q} \ln\left(\frac{N_A}{n_i}\right)$$

The depletion charge at maximum depletion width is given by Q_{dmax}, where ϵ_{Si} is the permittivity of Silicon

$$Q_{dmax} = \sqrt{2\,\epsilon_{Si}\,q\,N_A\,\phi_{sth}}$$

b) For "short" bulk (i.e. fully depleted)

As the bulk of the device is quite short, it is fully depleted before the maximum possible depletion depth is achieved. Hence the threshold voltage occurs when the device reaches its maximum depth of depletion layer, following which it goes into inversion. In this case, the threshold voltage is given by:

$$V_T = \phi_{ms} + \phi_s + \frac{Q_{dep}}{C_{piezo}}$$

In this scenario, the depletion charge, Q_{dep}, is given by

$$Q_{dep} = q\,N_A(2d - g)$$

The surface potential, which is obtained by integrating the charge Q_{dep} over the depletion region, which is the entire length of the Silicon layer, to obtain the E-field, which is then integrated to obtain the potential at the surface

$$\phi_s = \frac{q\,N_A(2d-g)^2}{2\,\varepsilon_{Si}} + \phi_{bg}$$

where ϕ_{bg} is the surface potential at the back gate and is itself dependent on the back gate voltage. This is responsible for the feed-through and we will ignore the AC modulation for now and calculate the surface potential at the back gate for the DC bias V_A.

$$\phi_{bg} = \frac{-2\,k\,T}{q} \ln\left(\frac{\phi_{ms} - V_A}{\gamma\sqrt{\frac{kT}{q}}}\right)$$

where γ is the body factor coefficient and is given by:

$$\gamma = \frac{1}{C_{piezo}}\sqrt{2\epsilon_{Si} q N_A}$$

2.5.4 Piezoelectric Contribution [16]

In a hexagonal crystal such as AlN, for an externally applied field E_3, dielectric constant, ε_3, direct piezoelectric coefficient matrix given by e and the inverse piezoelectric coefficient matrix given by d (as discussed in the previous section) and strain given by S, the electric displacement vector D_3 is given by

$$D_3 = \varepsilon_3 E_3 + d_{31}(S_1 + S_2) + d_{33}S_3 = \varepsilon_3 E_3 + e_{31}(S_1 + S_2) + e_{33}S_3$$

Assuming that the 1-D standing wave at resonance, $u(x,t)$, is only along the x direction which is also the direction along which the c-axis is oriented and the 33 coefficient is relevant, i.e. assuming that there is no strain along other two directions ($S_1 = S_2 = 0$). Thus we can rewrite above as

$$D_3 = \varepsilon_3 E_3 + d_{33}S_3$$

Since the contribution of the externally applied electric field is already accounted for as the term V_{GS} in the DC current equation for the sensing side, we set $E_3 = 0$ and we write

$$D_3 = e_{33}S_3$$

From this expression for the electric displacement, we may calculate the equivalent piezoelectrically induced Electric field, E_{piezo} and the corresponding voltage across the piezoelectric film, V_{piezo} as:

$$V_{piezo} = \int_{-d-g/2}^{-d+g/2} E_{piezo}(x)dx = -\frac{e_{33}}{\varepsilon_3}\int_{-d-\frac{g}{2}}^{-d+\frac{g}{2}} S_3(x)dx$$

$$V_{piezo} = -\frac{e_{33}}{\varepsilon_3}\int_{-d-\frac{g}{2}}^{-d+\frac{g}{2}} \frac{\partial u(x,t)}{\partial x}dx$$

$$= -\frac{e_{33}}{\varepsilon_3}\,\mathrm{U_0}\sin(k_n x)\cdot e^{j\omega_n t}\Big|_{-d-\frac{g}{2}}^{-d+\frac{g}{2}}$$

$$V_{piezo} = -\frac{e_{33}}{\varepsilon_3}\mathrm{U_0}\left[\sin\left(k_n\left(-d+\frac{g}{2}\right)\right) - \sin\left(k_n\left(-d-\frac{g}{2}\right)\right)\right]\cdot e^{j\omega_n t}$$

Again, reducing the bracket using the trigonometric identity,

$$\sin A - \sin B = 2\sin\frac{(A-B)}{2}\cos\frac{(A+B)}{2}$$

we get,

$$\sin\left(-k_n\mathrm{d}+\frac{k_n\mathrm{g}}{2}\right)-\sin\left(-k_n\mathrm{d}-\frac{k_n\mathrm{g}}{2}\right)= 2\sin\left(\frac{k_n\mathrm{g}}{2}\right)\cos\left(k_n\mathrm{d}\right)$$

Thus,

$$V_{piezo} = -2\frac{e_{33}}{\varepsilon_3}\mathrm{U}_0\cos(k_n d)\sin\left(k_n\frac{g}{2}\right)\cdot e^{j\omega_n t}$$

The transistor current in the linear regime, I_{DCLin} and in saturation, I_{DCsat} , as seen in the previous section is given by:

$$I_{DCLin} = \frac{H}{L_{gate}}\mu_n C_{piezo}(V_{GS} - V_T - \frac{V_{DS}}{2})V_{DS}$$

$$I_{DCsat} = \frac{H}{2\,L_{gate}}\mu_n C_{piezo}\,(V_{GS} - V_T)^2$$

Thus the V_{piezo} term simply contributes to an additional AC voltage on the sensing gate. Thus, in the linear regime, as long as the linear regime condition is satisfied with the net gate voltage ($V_{DS} \le V_G + V_{piezo} - V_T$) we can write the net current as a sum of the DC current, I_{DCLin}, and an AC component, i_{pelec}, as

$$I_{DCLin} + i_{peleclin} = \frac{H}{L_{gate}}\mu_n C_{piezo}(V_{GS} + V_{piezo} - V_T - \frac{V_{DS}}{2})V_{DS}$$

$$= I_{DCLin} + \frac{H}{L_{gate}}\mu_n C_{piezo}V_{piezo}V_{DS}$$

$$i_{peleclin} = \frac{H}{L_{gate}}\mu_n C_{piezo}V_{DS}V_{piezo}$$

$$= \frac{H}{L_{gate}}\mu_n C_{piezo}(V_{GS} - V_T - \frac{V_{DS}}{2})V_{DS}\frac{V_{piezo}}{(V_{GS} - V_T - \frac{V_{DS}}{2})}$$

This may be expressed in terms of the DC linear regime current as:

$$i_{peleclin} = I_{DCLin}\frac{V_{piezo}}{(V_{GS} - V_T - \frac{V_{DS}}{2})}$$

Similarly, in the saturation regime, ($V_{DS} \geq V_G + V_{piezo} - V_T$)

$$I_{DCsat} + i_{pelecsat} = \frac{H}{2\,L_{gate}} \mu_n C_{piezo} \left(V_{GS} + V_{piezo} - V_T\right)^2$$

$$= I_{DCsat} + \frac{H}{L_{gate}} \mu_n C_{piezo} V_{piezo} (V_{GS} - V_T) + \frac{H}{2\,L_{gate}} \mu_n C_{piezo} {V_{piezo}}^2$$

$$i_{pelecsat} = \frac{H}{L_{gate}} \mu_n C_{piezo} V_{piezo} (V_{GS} - V_T) + \frac{H}{2\,L_{gate}} \mu_n C_{piezo} {V_{piezo}}^2$$

$$= \frac{H}{2\,L_{gate}} \mu_n C_{piezo} (V_{GS} - V_T)^2 \frac{2\,V_{piezo}}{(V_{GS} - V_T)} + \frac{H}{2\,L_{gate}} \mu_n C_{piezo} (V_{GS} - V_T)^2 \frac{{V_{piezo}}^2}{(V_{GS} - V_T)^2}$$

This may be expressed in terms of the DC saturation current as:

$$i_{pelecsat} = I_{DCsat} \left(\frac{2\,V_{piezo}}{(V_{GS} - V_T)} + \frac{{V_{piezo}}^2}{(V_{GS} - V_T)^2} \right)$$

2.5.5 Piezoresistive Contribution

The standing wave along the x-direction in the resonator results in a time-dependent strain along the channel which modulates the mobility due to the piezoresistive effect [18]. From the previous section, we may express this as:

$$\frac{\Delta\mu_n}{\mu_n} = \pi_{111}\, E_{Si}\; S_3(x)|_{x=-d+\frac{g}{2}} = \pi_{111}\, E_{Si}\; k_n\, \mathrm{U}_0 \cos\left(-k_n d + \frac{k_n g}{2}\right)$$

In the linear regime, we have,

$$I_{DCLin} + i_{preslin} = \frac{H}{L_{gate}} (\mu_n + \Delta\mu_n) C_{piezo} \left(V_{GS} - V_T - \frac{V_{DS}}{2}\right) V_{DS}$$

$$= \frac{H}{L_{gate}} \mu_n C_{piezo} \left(V_{GS} - V_T - \frac{V_{DS}}{2}\right) V_{DS} \left(1 + \frac{\Delta\mu_n}{\mu_n}\right)$$

$$= I_{DClin} + I_{DClin} \frac{\Delta\mu_n}{\mu_n}$$

$$i_{preslin} = I_{DClin} \frac{\Delta\mu_n}{\mu_n} = I_{DClin} \pi_{111}\, E_{Si}\; k_n\, \mathrm{U}_0 \cos\left(-k_n d + \frac{k_n g}{2}\right)$$

Similarly in the saturation regime,

$$i_{pressat} = I_{DCsat}\frac{\Delta\mu_n}{\mu_n} = I_{DCsat}\,\pi_{111}\,E_{Si}\,k_n\,U_0\cos\left(-k_n d + \frac{k_n g}{2}\right)$$

The sign of the piezoresistive coefficient along the direction of the current determines whether this contribution is in phase or out of phase with the piezoelectric contribution.

2.5.6 Capacitive Contribution

Apart from the piezoelectric contribution to the output AC current, we will also have an AC current resulting from the change in the capacitance of the piezoelectric film. The insulating AlN film forms a capacitor which squeezes and expands due to the acoustic wave, and this results in an additional AC current. Thus, this current is positive when the capacitance increases, i.e. when the piezoelectric film is compressed. Calculating the capacitance at DC, C_{piezo}, and at the maximum amplitude of resonance, C'_{piezo}, where the piezoelectric film expands to thickness $g + \Delta g$, we have,

$$C_{piezo} = \frac{\varepsilon_0\, k_{piezo}}{g}$$

$$C'_{piezo} = \frac{\varepsilon_0\, k_{piezo}}{g + \Delta g}$$

Thus, the change in capacitance, ΔC_{piezo}, assuming Δg is small, is given by:

$$\Delta C_{piezo} = C'_{piezo} - C_{piezo} = \frac{\varepsilon_0\, k_{piezo}}{g} - \frac{\varepsilon_0\, k_{piezo}}{g + \Delta g} = \frac{\varepsilon_0\, k_{piezo}}{g + \Delta g}\frac{\Delta g}{g} \approx \frac{\varepsilon_0\, k_{piezo}\Delta g}{g^2}$$

We now calculate the net increase in the thickness of the piezoelectric film, Δg, by integrating the strain function over the thickness of the film

$$\Delta g = \int_{-d-\frac{g}{2}}^{-d+\frac{g}{2}} \frac{du(x)}{dx}dx = U_0 e^{j\omega_n t}\sin(k_n x)\Big|_{-d-\frac{g}{2}}^{-d+\frac{g}{2}}$$

$$\Delta g = U_0 e^{j\omega_n t}\left\{\sin\left(k_n\left(-d + \frac{g}{2}\right)\right) - \sin\left(k_n\left(-d - \frac{g}{2}\right)\right)\right\}$$

Again, reducing the second bracket using the trigonometric identity,

$$\sin A - \sin B = 2\sin\frac{(A-B)}{2}\cos\frac{(A+B)}{2}$$

we get,

$$\sin\left(-k_n\mathrm{d}+\frac{k_n\mathrm{g}}{2}\right)-\sin\left(-k_n\mathrm{d}-\frac{k_n\mathrm{g}}{2}\right)= 2\sin\left(\frac{k_n\mathrm{g}}{2}\right)\cos\left(k_n\mathrm{d}\right)$$

Thus we get,

$$\Delta g = 2\,\mathrm{U}_0 e^{j\omega_n t}\sin\left(\frac{k_n\mathrm{g}}{2}\right)\cos\left(k_n\mathrm{d}\right)$$

$$\Delta C_{piezo} = \frac{2\,\varepsilon_0\,k_{piezo}}{g^2}\mathrm{U}_0 e^{j\omega_n t}\sin\left(\frac{k_n\mathrm{g}}{2}\right)\cos\left(k_n\mathrm{d}\right)$$

In the linear regime, we have,

$$I_{DCLin} + i_{caplin} = \frac{H}{L_{gate}}\mu_n\left(C_{piezo}+\Delta C_{piezo}\right)\left(V_{GS}-V_T-\frac{V_{DS}}{2}\right)V_{DS}$$

$$= \frac{H}{L_{gate}}\mu_n C_{piezo}\left(V_{GS}-V_T-\frac{V_{DS}}{2}\right)V_{DS}\left(1+\frac{\Delta C_{piezo}}{C_{piezo}}\right)$$

$$= I_{DCLin} + I_{DCLin}\frac{\Delta C_{piezo}}{C_{piezo}}$$

$$i_{caplin} = I_{DCLin}\frac{\Delta C_{piezo}}{C_{piezo}} = I_{DCLin}\frac{2\,\varepsilon_0\,k_{piezo}}{g^2}\mathrm{U}_0 e^{j\omega_n t}\sin\left(\frac{k_n\mathrm{g}}{2}\right)\cos(k_n\mathrm{d})$$

Similarly in the saturation regime,

$$i_{capsat} = I_{DCsat}\frac{\Delta C_{piezo}}{C_{piezo}} = I_{DCsat}\frac{2\,\varepsilon_0\,k_{piezo}}{g^2}\mathrm{U}_0 e^{j\omega_n t}\sin\left(\frac{k_n\mathrm{g}}{2}\right)\cos(k_n\mathrm{d})$$

The total modulation current in the linear or the saturation regime is thus given by summing these three contributions in that regime:

$$i_{out} = i_{pelec} + i_{pres} + i_{cap}$$

Now that we have completed the full analysis for this device, we will look at the relative contributions of different mechanisms to the drive and sense side. This will help characterize and optimize the performance of the device.

OPTIMIZATION

3.1 Assumed Values

Given the set of equations in the previous section, we can make calculations regarding the expected performance of the piezoelectric RBT. For this, we assume the following default values for the device.

3.1 Table of Assumed Constants [7, 8, 17, 18, 19, 20]

Parameter	Value
V_D	1 V
V_G	5 V
V_A	-5 V
v_{ac}	0.1 V
g	10^{-7} m or 100 nm
Q_{33}	0.92 m^4/C^2
E_{Si}	$170 * 10^9$ N/m^2
E_{piezo}	$135 * 10^9$ N/m^2
E_{Mo}	$329 * 10^9$ N/m^2
L_{Mo}	$2 * 10^{-7}$ m or 200 nm
ρ_{Si}	2330 kg/m^3
ρ_{piezo}	3200 kg/m^3
ρ_{Mo}	10280 kg/m^3
ε_0	$8.85 * 10^{-12}$ F/m
k_{piezo}	8.9
L_{gate}	500 nm
H	1 um
W	$L_{gate} + 2\ \mu m$
μ_n	$100 * 10^{-4}\ V/m^2s$
ϵ_{Si}	11.6
q	$1.6* 10^{-19}$C
N_A	$10^{20}/m^3$
k	$1.38 * 10^{-23} J/K$
T	300 K
n_i	$1.08 * 10^{16}/m^3$
π_{111}	$45 * 10^{-11} m^2/N$
Q	1000

Piezoelectric Coefficients for AlN [7]

$$e = \begin{bmatrix} 0 & 0 & 0 & 0 & -0.48 & 0 \\ 0 & 0 & 0 & -0.48 & 0 & 0 \\ -0.58 & -0.58 & 1.55 & 0 & 0 & 0 \end{bmatrix} (\text{C/m\^2})$$

$$d = \begin{bmatrix} 0 & 0 & 0 & 0 & -4 & 0 \\ 0 & 0 & 0 & -4 & 0 & 0 \\ -1.98 & -1.98 & 4 & 0 & 0 & 0 \end{bmatrix} 10^{-12} (\text{C/N})$$

3.2 Driving Side

Using the values from Table [3.1], the relative amplitude of the piezoelectric and electrostrictive stress (AC) is given by:

$$\frac{\sigma_p}{\sigma_e} = \frac{e_{33}\, g}{E_{piezo}\, Q_{33} \varepsilon_0^2 \left(k_{piezo} - 1\right)^2 (V_A - V_D)} \approx 150$$

Thus the piezoelectric stress is more than two orders of magnitude greater than that due to electrostriction hence the latter will be ignored in subsequent analysis.

Using the piezoelectric-only drive, we get the following plot [Figure 3.1] for the gate voltage induced due to the piezoelectric film, V_{piezo}, with respect to time during one time period.

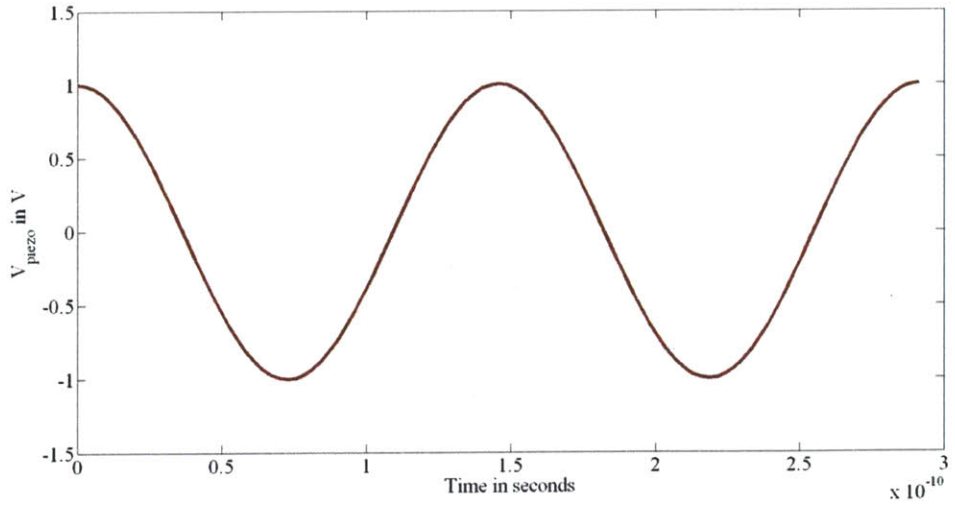

Figure 3.1 Plot of piezoelectrically induced voltage V_{piezo} vs one time period

3.3 Sensing Side

The plot shows that the induced voltage varies between -1V and 1V for default values. For a gate voltage of 5V, threshold voltage < 1V and drain voltage of 1V, this also means that the transistor is always in saturation for these default values. In this case, on the sensing side, we have the relative magnitude of the piezoelectric and the piezoresistive contribution in saturation given by:

$$\frac{i_{pelecsat}}{i_{pressat}} = \frac{\left(\frac{2\,V_{piezo}}{(V_{GS} - V_T)} + \frac{{V_{piezo}}^2}{(V_{GS} - V_T)^2}\right)}{\pi_{111}\,E_{Si}\;k_n\,\mathrm{U}_0\cos\left(-k_n d\;+\;\frac{k_n g}{2}\right)} \approx 12$$

In the linear regime, the relative amplitude is given by:

$$\frac{i_{peleclin}}{i_{preslin}} = \frac{\frac{V_{piezo}}{(V_{GS} - V_T - \frac{V_{DS}}{2})}}{\pi_{111}\,E_{Si}\;k_n\,\mathrm{U}_0\cos\left(-k_n d\;+\;\frac{k_n g}{2}\right)}$$

and the relative magnitude depends on the values set for V_{GS} and V_{DS}. Thus for now we say that both the piezoelectric and piezoresistive effects have a non-negligible contribution to the output current.

The relative magnitude of the piezoresistive and the capacitive contribution in the saturation as well as the linear regimes are given by:

$$\frac{i_{pres}}{i_{cap}} = \frac{\pi_{111}\,E_{Si}\;k_n\cos\left(-k_n d\;+\;\frac{k_n g}{2}\right)}{\frac{2\,\varepsilon_0\,k_{piezo}}{g^2}\sin\left(\frac{k_n g}{2}\right)\cos\left(k_n \mathrm{d}\right)} \approx 10^5$$

Thus we can ignore the capacitive contribution while setting up the equations on the sensing side.

3.4 Equivalent Circuit Model

With the above analysis in place, we can finally draw and equivalent circuit model of the Piezoelectric RBT which is based on the π model used for transistor analysis [Figure 3.2]. For the piezoelectric RBT, we modify the traditional model by introducing the acoustic transconductance g_{ma} which gives rise to a

high-Q voltage-dependent current source controlled by the driving gate voltage.

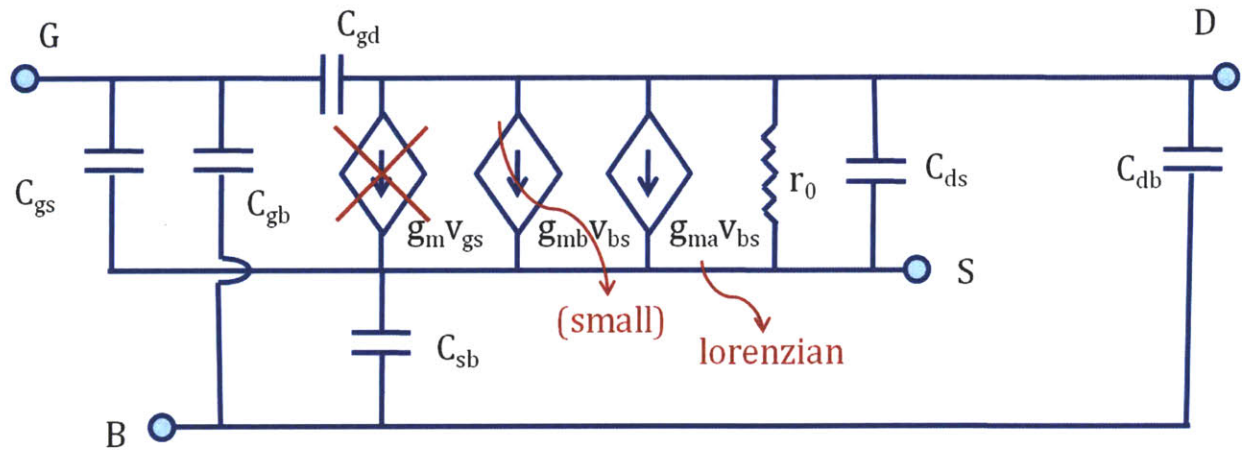

Figure 3.2: Equivalent circuit model for Piezoelectric RBT showing the gate (G), drain (D), source (S) and back gate (B) terminals, capacitances (C) and voltage dependent current sources with transconductance (g).

We may express this transconductance, g_{ma}, or the equivalent resistance at resonance, R_X, in terms of the output current, i_{out} and the driving voltage, v_{ac} as:

$$R_X = \frac{1}{g_{ma}} = \frac{v_{ac}}{Amplitude(i_{out})}$$

3.5 Trends in i_{out}

We set up equations to plot the total AC output current i_{out} vs time. Two of the important control parameters are V_{GS} and V_{DS} and we first observe the effect of changing those on the AC output current.

In Figure [3.3] the non-linearity for small values of the gate voltage occurs because the net gate voltage, which is given by $V_{GS} + V_{piezo}$ switches between saturation, linear and sub-threshold regimes. For the net gate voltage to be permanently in the saturation regime, we require, $V_{GS} - V_{piezo} - V_T > V_{DS}$. For a threshold voltage $V_T = 0.7V$, $V_{DS} = 1V$, and $V_{piezo} = 1V$, the DC gate bias $V_{GS} \geq 2.7V$ which agrees well with the plot. Higher gate bias voltages lead to larger AC output current as the DC bias current

I_{DCsat} increases with V_{GS} in saturation, and the piezoelectric contribution to the AC output current also increases linearly with V_{GS} following the transistor equations:

$$I_{DCsat} = \frac{H}{2\,L_{gate}}\,\mu_n C_{piezo}\,(V_{GS} - V_T)^2$$

$$i_{pelecsat} = \frac{H}{L_{gate}}\,\mu_n C_{piezo} V_{piezo}(V_{GS} - V_T) + \frac{H}{2\,L_{gate}}\,\mu_n C_{piezo} {V_{piezo}}^2$$

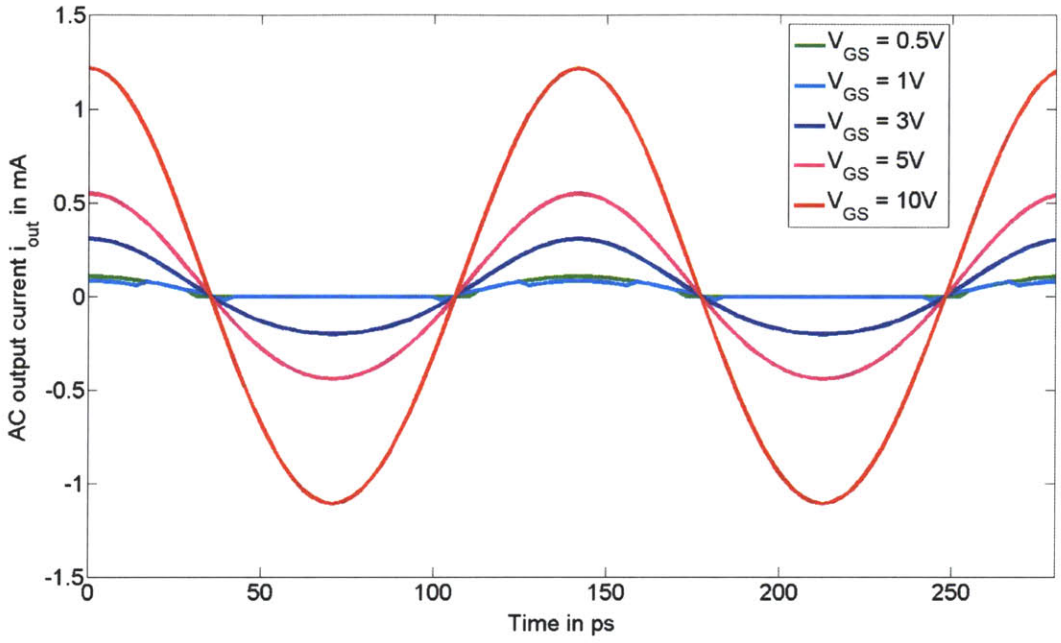

Figure 3.3: Plot of i_{out} vs time for varying gate bias voltage V_{GS} showing non-linearity for small V_{GS}.

Thus, the higher the gate voltage, the higher the DC as well as AC output current, which leads to a higher transconductance and lower insertion loss for the device. The upper limit on this is that a large V_{GS} will lead to a large leakage current through the piezoelectric film and ultimately result in its breakdown.

We now plot the output current as a function of the drain voltage V_{DS} as shown in Figure [3.4]. For small values of V_{DS} (< 3.3V), the condition $V_{GS} - V_{piezo} - V_T > V_{DS}$ is always true for the known values of the $V_{GS} = 5V$, $V_{piezo} = 1V$ and $V_T = 0.7\,V$ and the transistor remains in saturation and no dependence on V_{DS} is observed as expected from the transistor equations. For intermediate values of V_{DS} (between 3.3 V

and 5.3 V), the transistor switches back and forth between the saturation and linear regimes when V_{piezo} is near its peak values and a distortion in the output waveform is observed. For high values of V_{DS}, the condition $V_{GS} - V_{piezo} - V_T < V_{DS}$ is always true, pushing the transistor into the linear regime where the dominant component of the AC output current, $i_{peleclin}$, is dependent on V_{DS} through the relation:

$$i_{peleclin} = \frac{H}{L_{gate}} \mu_n C_{piezo} V_{DS} V_{piezo}$$

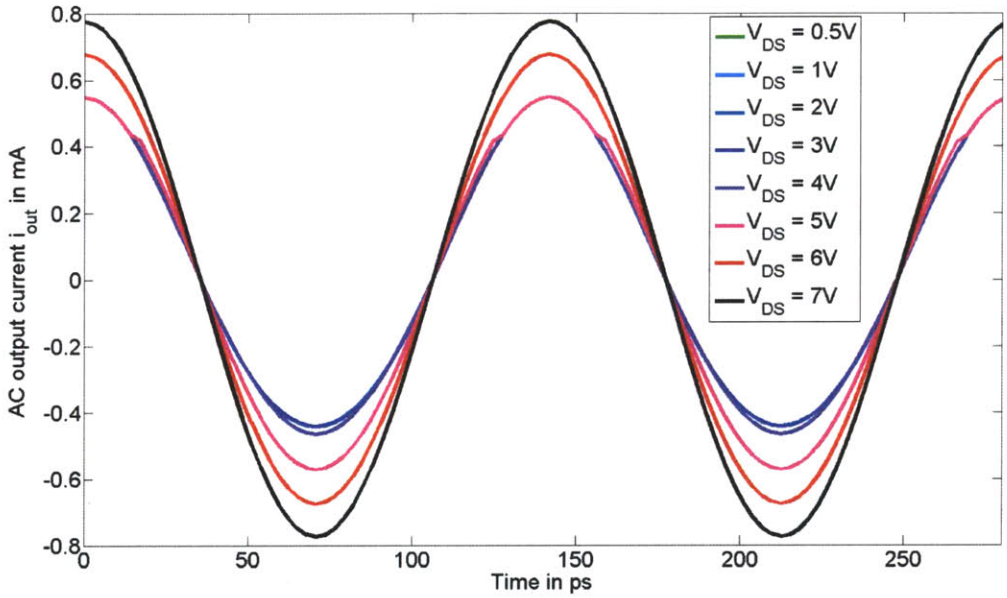

Figure 3.4: Plot of i_{out} vs time for varying drain-source voltage V_{DS} showing non-linearity for large V_{DS}.

Thus, for a sinusoidally varying output AC current the transistor must remain in the saturation or linear regimes. However, for a fixed drain voltage, the piezoelectrically modulated AC current in the linear regime is smaller than that in the saturation regime if:

$$i_{pelecsat} = \frac{H}{L_{gate}} \mu_n C_{piezo} V_{piezo} (V_{GS} - V_T) + \frac{H}{2\,L_{gate}} \mu_n C_{piezo} {V_{piezo}}^2 > \frac{H}{L_{gate}} \mu_n C_{piezo} V_{DS} V_{piezo}$$

iff

$$(V_{GS} - V_T) + \frac{V_{piezo}}{2} > V_{DS}$$

From Figures [3.3] and [3.4], we conclude that the output signal may be maximized by applying high gate and drain voltages to the device, the tradeoff being the limitations imposed by the application.

We next plot the AC output current, i_{out}, as a function of the quality factor in Figure [3.5]. The increasing amplitude of i_{out} with Q can be explained by the fact that a larger Q value means that the amplitude of vibrations at resonance is amplified more, leading to a larger i_{out} due to both piezoelectric and piezoresistive effects. The plot however shows that the distortion of the output waveform from a sinusoidal also becomes more severe with increasing Q, thus requiring a tradeoff to be considered for device design. The quality factor is a variable determined by anchor loss, thermoelastic damping and phonon-phonon scattering and can be improved by using optimal materials and improved fabrication techniques such as Molecular Beam Epitaxy [21, 22].

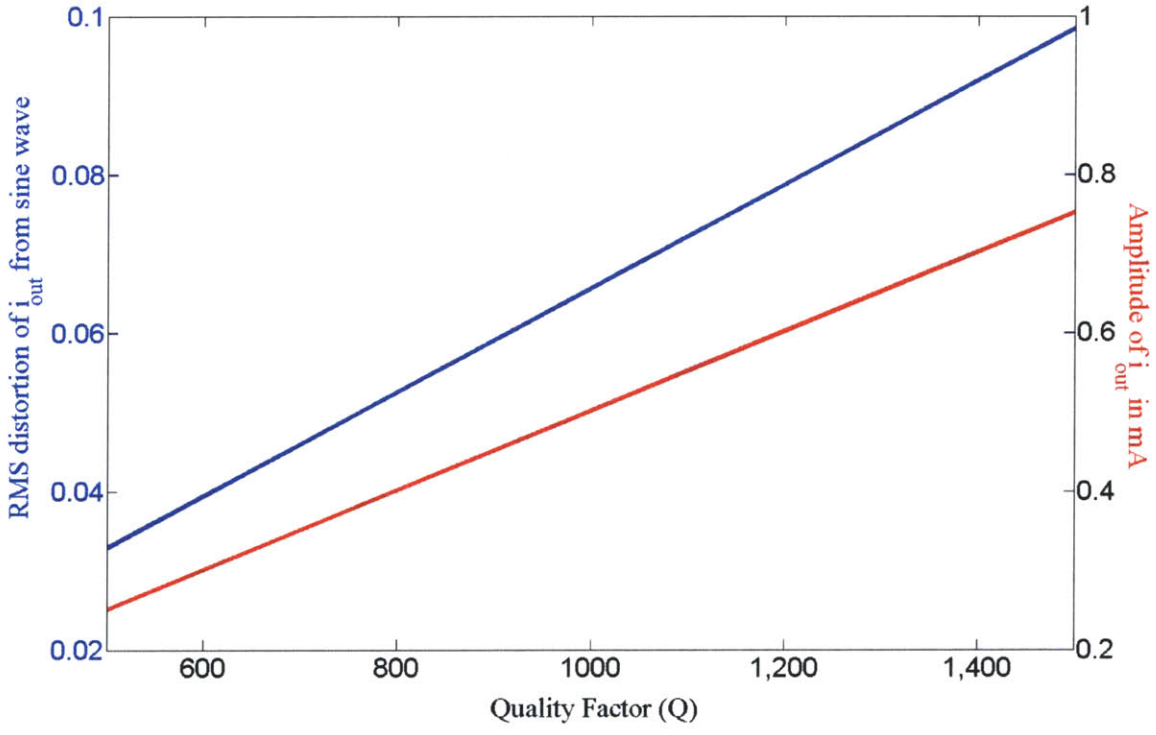

Figure 3.5: Plot of i_{out} vs time for varying Quality factor (Q)

The next parameter that may be considered is the length of the gate, the relevant plot for which is Figure [3.6]. As expected, the output current non-linearly decreases with gate length as the equations clearly show the dominant terms $i_{pelecsat}$ and $i_{peleclin}$ are inversely proportional to the length of the gate. However, a factor that is not accurately captured by the equations is that long narrow (more 1D) devices usually show better suppression of spurious modes and a purer filter spectrum as a result of this which is a highly desirable characteristic in a bandpass filter.

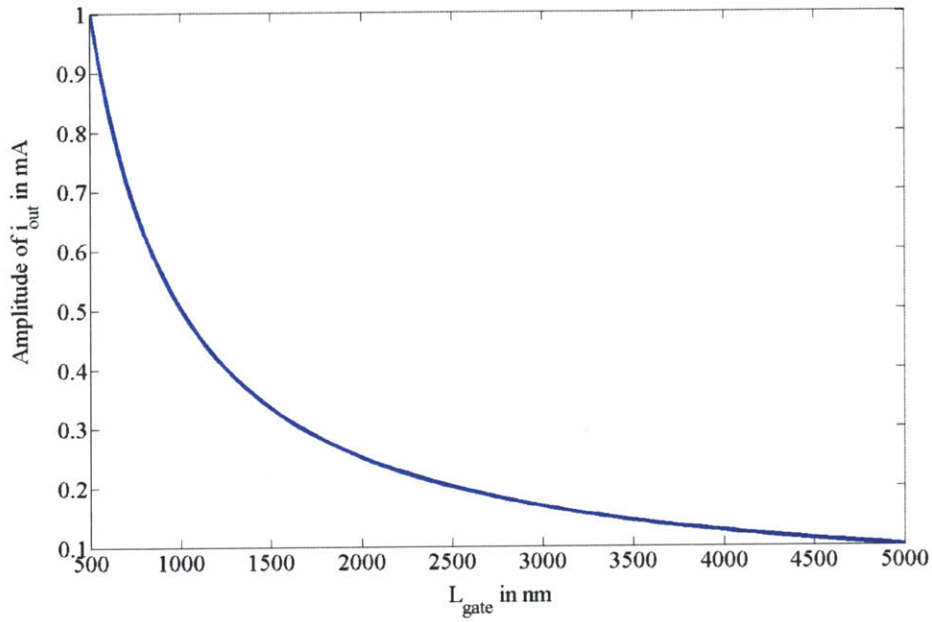

Figure 3.6: Plot of the amplitude of i_{out} vs varying length of gate (L_{gate})

The next parameter that may be considered is the position of the piezoelectric films with respect to the device (d), the relevant plot for which is Figure [3.7]. We immediately notice two things from this figure; first, the frequency of the device changes as we vary the length of the Silicon body of the transistor. This observation makes sense as our frequency is a function of the Silicon body length and as the length of the bulk increases, the device becomes longer and the corresponding frequency decreases. Secondly, we observe that the output current i_{out} does not vary monotonically with d. This optimization of the film position will be further investigated in the next section.

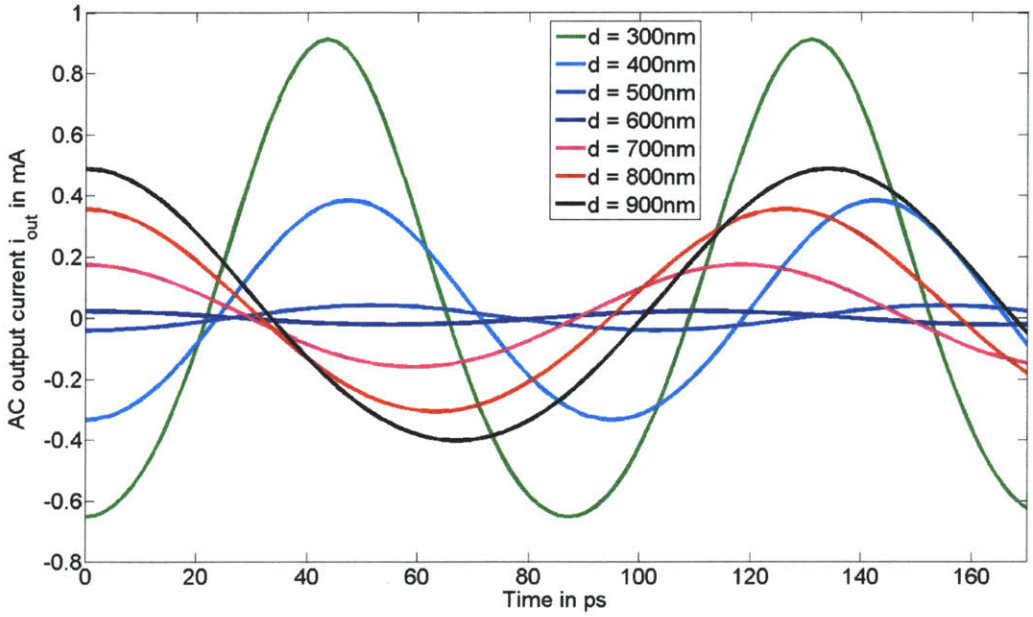

Figure 3.7: Plot of i_{out} vs time for varying position of piezoelectric films (d) with respect to the center of the device

The final plot we consider is of i_{out} vs. time with varying thickness of piezoelectric film (g), as shown in Figure [3.8]. Again, we observe that the time period or the frequency varies with thickness of the piezoelectric. This is because the thickness influences the effective Young's Modulus, density and acoustic velocity of the device as discussed in section [2.4]. Thus, holding the length of the bulk Si region and the Moly electrodes constant, the frequency increases as the piezoelectric film grows thinner and the resonant dimension becomes shorter in length. Secondly, we observe that the magnitude of i_{out} increases as g decreases. On the driving side, the piezoelectric driving stress increases as the same voltage v_{ac} is applied across a thinner film, resulting in a larger Electric field. On the sensing side, the thinner film results in a larger C_{piezo} which results in a higher overall DC current leading to a larger AC modulation.

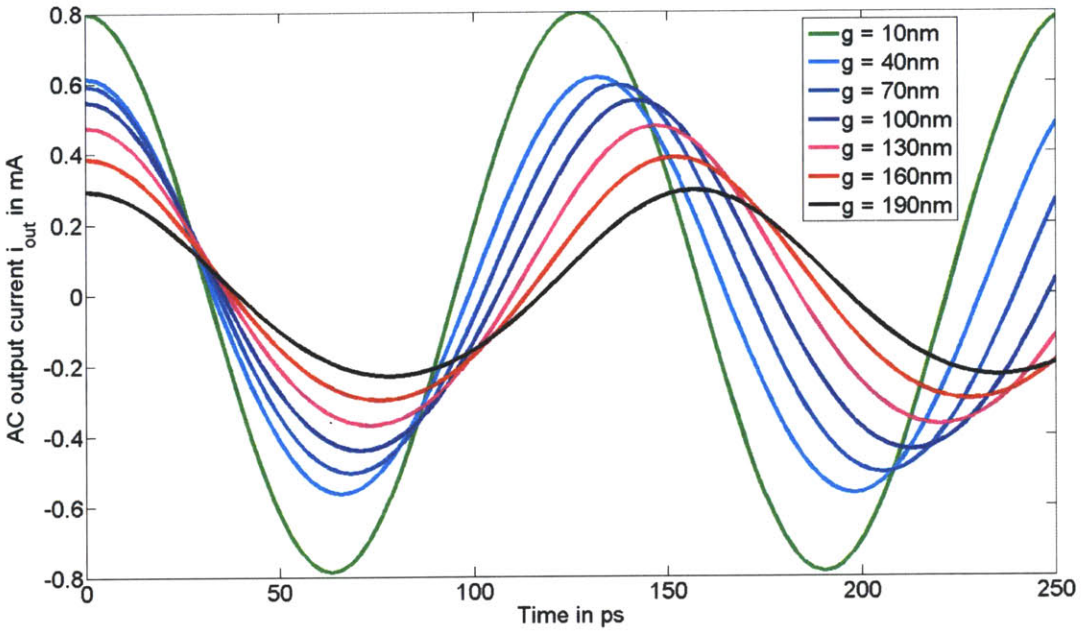

Figure 3.8: Plot of i_{out} vs time for varying thickness of piezoelectric (g)

In summary, it is clear from the plots above that the gate and drain voltages V_{GS} and V_{DS} are an effective method to tweak the output current modulation and in general we get a higher output signal as long as we remain in saturation for a given V_{GS}. Higher bias voltages ultimately limit the applications of the device, hence it would be interesting to explore the tradeoff in further detail. The gate length L_{gate} in general needs to be small but is ultimately limited by fabrication tolerances, however a tradeoff exists here too as a longer device would ultimately reduce spurious modes. The transistor equations we have used are also applicable only for a "long" channel FET. Increasing the Q is another effective way to increase the current modulation and can be improved by material choice and improved fabrication techniques. The thickness of the piezoelectric film (g) as well as its position from the center of the device (d) are both parameters that may be optimized for specific resonator performance characteristics.

3.6 Comparison with a Traditional Piezoelectric Resonator

Before we optimize for the above parameters, it is worth comparing the Piezoelectric RBT with a traditional resonator with piezoelectric drive and sense as shown in Figure [3.9]. Comparing this with the schematic of the Piezoelectric RBT in Figure [2.1], it is obvious that the traditional resonator has a similar mechanical structure as the RBT but lacks the FET sensing which is possible only through the source and drain regions. The primary advantage to this structure is that it is easier to fabricate as it does not require an additional step to dope the source and drain.

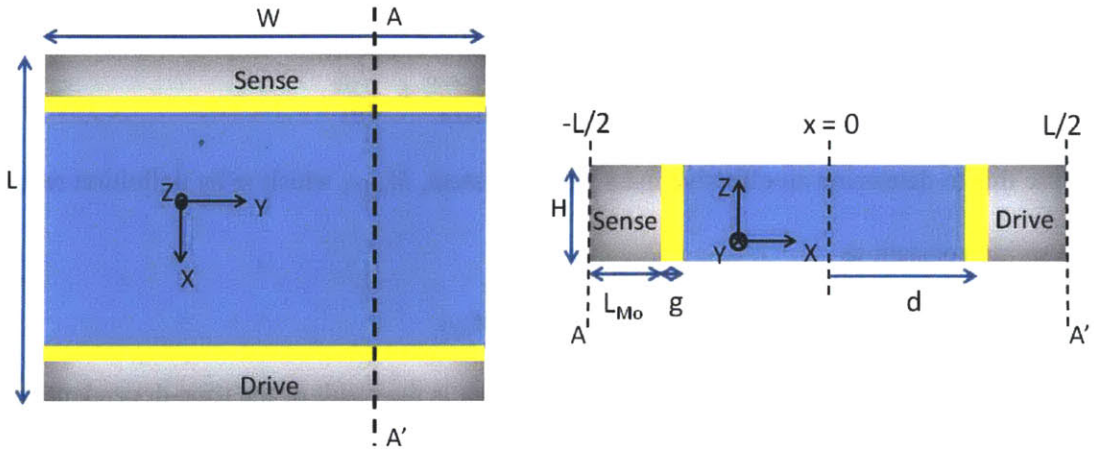

Figure 3.9: (*a*) Schematic of traditional piezoelectric drive and sense based resonator. The piezoelectric films are sandwiched between a Silicon body and conductive electrodes but no source or drain are present. (*b*) Cross section along A-A' line.

We compare the piezoelectric RBT with a traditional piezoelectric resonator with a piezoelectric drive and sense without FET-based sensing. For this analysis, we assume the physical structure is the same as [Figure 2.1] without the source and drain regions on either side. An actuation voltage of $V_A + v_{ac}$ is applied on the driving gate, the body is grounded and a DC voltage V_G is applied on the sensing gate similar to the case of the piezoelectric RBT.

In this case, the drive side equations are the same as the Piezoelectric RBT as derived in Section [2.3] with the driving stress arising from piezoelectricity and electrostriction. The wave equations are also the

same as discussed in Section [2.4] as the mechanical structure is assumed to be identical as well. A relevant derivation to note here is the calculation of the effective spring constant, k_{eff}, as

$$k_{eff} = \frac{E_{eff}\, W\, H}{L}$$

Where the effective Young's modulus, E_{eff}, was determined as

$$E_{eff} = \frac{L}{\frac{2\, L_{Mo}}{E_{Mo}} + \frac{2\, L_{piezo}}{E_{piezo}} + \frac{L_{Si}}{E_{Si}}}$$

Thus we have

$$k_{eff} = \frac{W\, H}{\frac{2\, L_{Mo}}{E_{Mo}} + \frac{2\, L_{piezo}}{E_{piezo}} + \frac{L_{Si}}{E_{Si}}}$$

We can use this to determine an effective mass for the system, M_{eff}, which is by definition related to the effective spring constant as

$$k_{eff} = \omega_n^2\, M_{eff}$$

For a traditional piezoelectric resonator, the sensing current is the result of the time-dependent charge that accumulates at the piezoelectric film as a result of its vibrations. As for the piezoelectric RBT, we have for an externally applied field E_3, dielectric constant, ε_3, direct piezoelectric coefficient matrix given by e and the inverse piezoelectric coefficient matrix given by d (as discussed in the previous section) and strain given by S, the electric displacement vector D_3 is given by

$$D_3 = \varepsilon_3 E_3 + e_{31}(S_1 + S_2) + e_{33} S_3 = \varepsilon_3 E_3 + e_{31}(S_1 + S_2) + e_{33} S_3$$

Assuming a 1-D standing wave at resonance and $S_1 = S_2 = 0$, and ignoring the externally applied DC field E_3 we can rewrite the above as

$$D_3 = e_{33} S_3$$

As calculated in Section [2.] we get the corresponding voltage across the piezoelectric film, V_{piezo} as:

$$V_{piezo} = -2\frac{e_{33}}{\varepsilon_3} \mathrm{U}_0 \cos(k_n d) \sin\left(k_n \frac{g}{2}\right) \cdot e^{j\omega_n t}$$

We now calculate the induced charge at the gate, Q_{piezo}, using the capacitive equation

$$Q_{piezo} = C_{piezo}\, V_{piezo}$$

$$Q_{piezo} = -2\,\frac{WH\varepsilon_3}{g}\frac{e_{33}}{\varepsilon_3}\mathrm{U}_0\cos(k_n d)\sin\left(k_n\,\frac{g}{2}\right)\cdot e^{j\omega_n t}$$

The output current i_{out} is given by

$$i_{out} = \frac{dQ_{piezo}}{dt} = -j\omega_n\,\frac{2WH}{g}e_{33}\,\mathrm{U}_0\cos(k_n d)\sin\left(k_n\,\frac{g}{2}\right)\cdot e^{j\omega_n t}$$

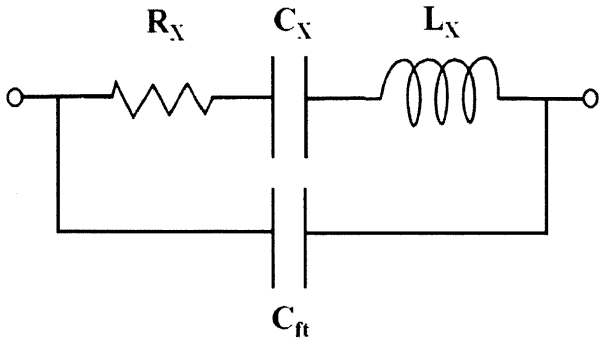

Figure 3.10: Butterworth Van dyke (BVD) model of resonator showing equivalent electrical circuit

The equivalent motional impedance R_X is given by

$$R_X = \frac{v_{ac}}{i_{out}}$$

We now calculate the other equivalent circuit parameters for the BVD model [23], namely the equivalent motional inductance L_X and capacitance C_X so that the resonator may be simulated as an equivalent RLC circuit over a range of frequencies [Figure 3.10]. We first calculate the transduction efficiency η which is related to the motional impedance R_X and the effective mass M_{eff} as

$$\eta^2 = \frac{M_{eff}\,\omega_n}{R_X\,Q}$$

We then calculate the L_X and C_X as follows

$$C_X = \frac{\eta^2}{k_{eff}}$$

$$L_X = \frac{M_{eff}}{\eta^2}$$

Using the assumed constants from Table 3.1, we generate a frequency sweep around the frequency of operation using MATLAB Simulink. The result is shown in Figure [3.11]

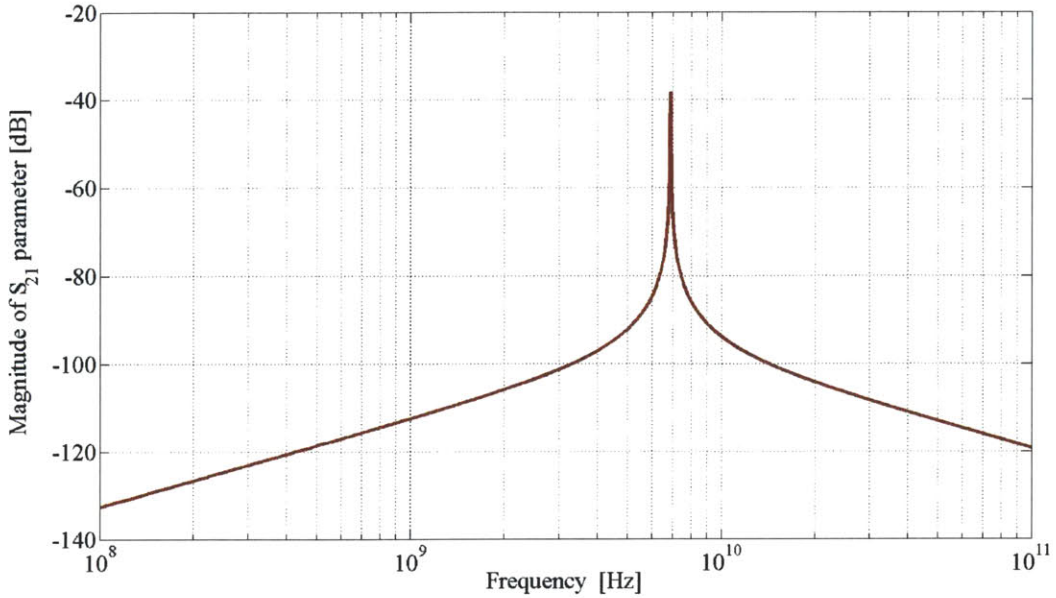

Figure 3.11 : Frequency sweep showing the S_{21} parameter for the traditional piezoelectric resonator around the frequency of operation assuming a 50 Ω load.

3.7 Trends in R_X

We now return to the performance characterization of the Piezoelectric RBT, comparing it with the additional traditional piezoelectric resonator. For the traditional resonator, we use the same table of assumed constants [Table 3.1] as for the Piezoelectric RBT. We first plot the R_X as a function of the gate voltage V_{GS} as shown in Figure [3.12].

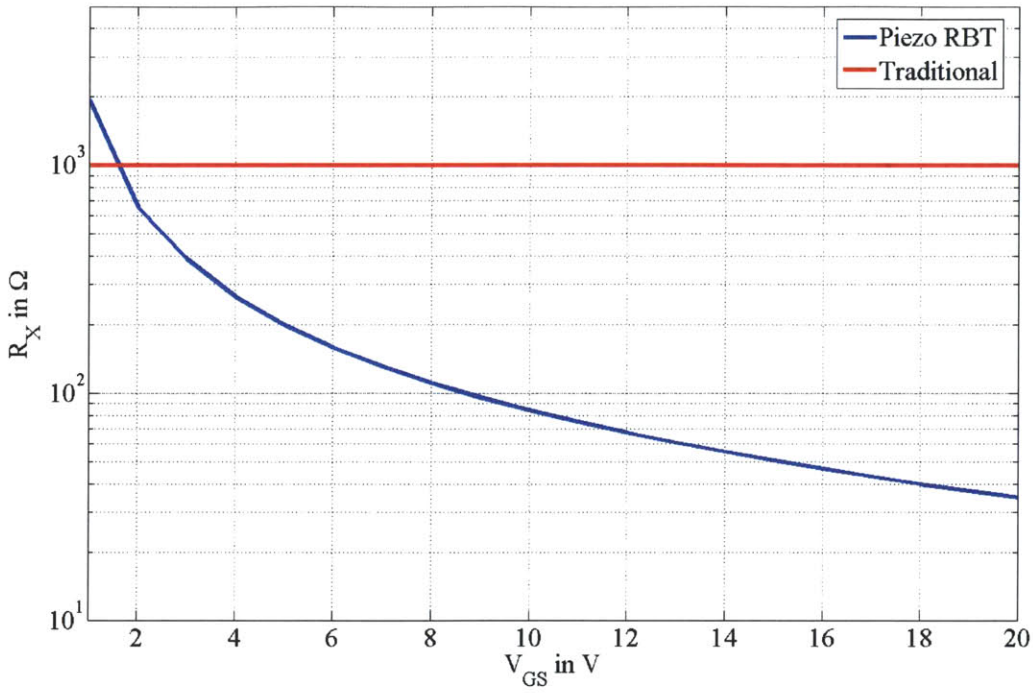

Figure 3.12: Plot of R_X as a function of the gate voltage V_{GS} for piezoelectric RBT and traditional piezoelectric resonator.

As the gate voltage V_{GS} does not figure in the traditional piezoelectric device equations, we see its R_X is at a constant value. On the other hand, for the piezoelectric RBT, we see that the R_X drops sharply with the gate voltage V_{GS} and on the plot above gets to very low values (~ 20 Ω) around 20V. Thus the piezoelectric RBT has a lower motional impedance than the traditional resonator at all values of the gate voltage. Having to apply very high voltages certainly limits the device in terms of potential applications and hence a tradeoff on this front will have to be considered with specific applications in mind.

Keeping the gate voltage at its previous value of 5 V, we now plot the R_X as a function of the position of the piezoelectric films with respect to the center of the device (d) as shown in Figure [3.13]. For this plot however, rather than keeping the thickness of the Mo electrodes constant at 200 nm as for plot [3.7], we keep the operating frequency constant at 5 GHz from an application point of view.

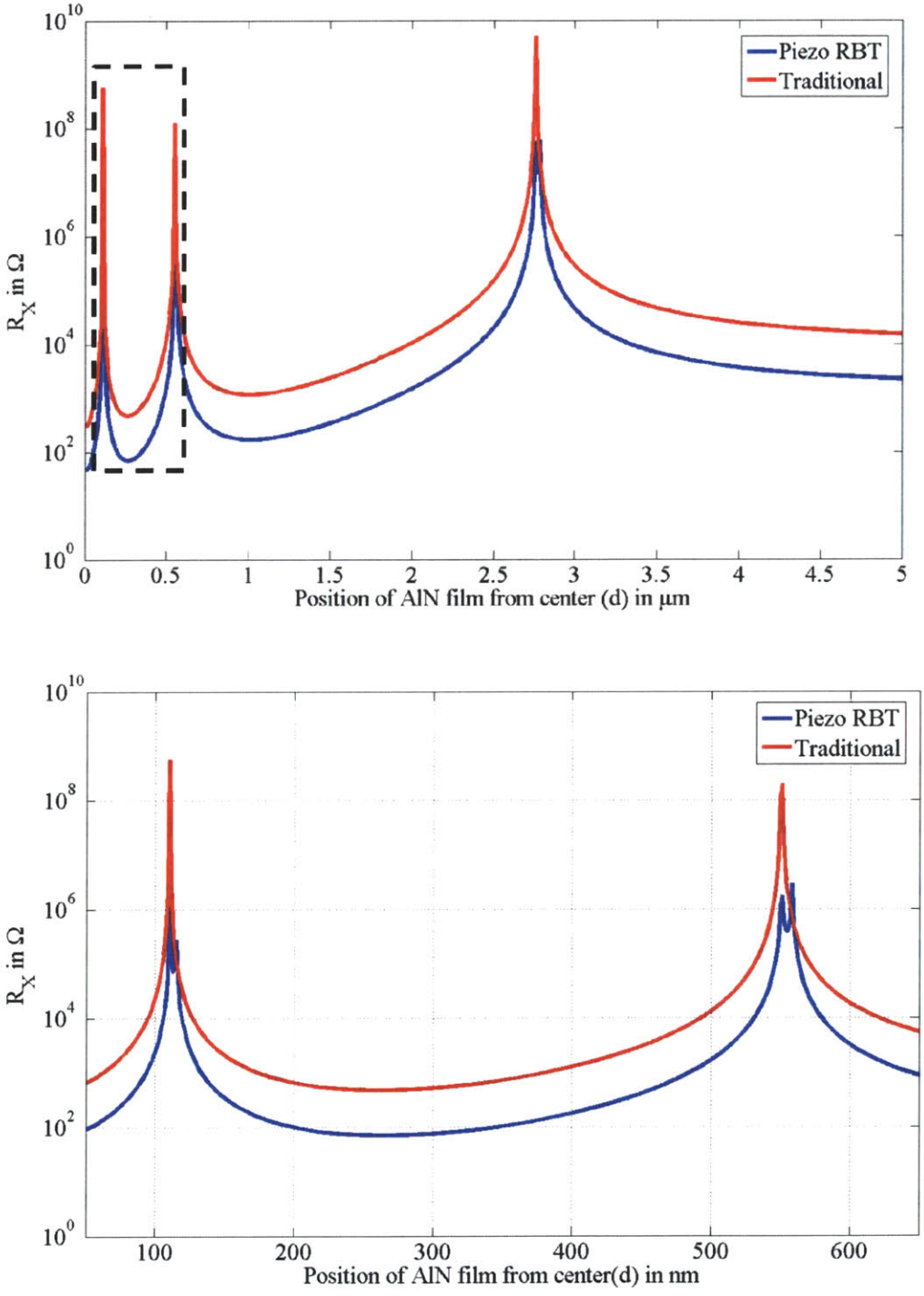

Figure 3.13: (top) Plot of R_X as a function of the position of the piezoelectric films from the center of the device (d) for device operating in third harmonic $n = 3$ for piezoelectric RBT and traditional piezoelectric resonator having a 100 nm AlN film and operating at 5 GHz (bottom) Zooming in on plot on top, showing a range where d optimized for R_X

The R_X of the Piezoelectric RBT is about an order of magnitude lower than that of the traditional piezoelectric resonator when the film position is optimized to minimize R_X. As expected from the current modulation plot, the amplitude of the AC output current as well as the impedance R_X does not change monotonically with the position of the piezoelectric film position with respect to the center of the device. in this case, the optimal value of R_X seems to occur for $d = 250\ nm$. To understand the periodicity of the trend better, we try plotting the above again for the 9th harmonic instead as shown in Figure [3.14]. The number of minima is related to the harmonic number which may be explained by the fact that the AC saturation current i_{out} is a function of the piezoelectrically induced voltage V_{piezo}, which in turn is a sinusoidal function of the AlN film position and the wavenumber k_n as shown earlier:

$$i_{pelecsat} = I_{DCsat}\left(\frac{2\,V_{piezo}}{(V_{GS} - V_T)} + \frac{{V_{piezo}}^2}{(V_{GS} - V_T)^2}\right)$$

$$V_{piezo} = -2\frac{e_{33}}{\varepsilon_3}\mathrm{U}_0 \cos(k_n d)\sin\left(\frac{k_n \mathrm{g}}{2}\right)\cdot e^{j\omega_n t}$$

$$\mathrm{U}_0 = = \frac{2\sigma_{\mathrm{drive}}}{\mathrm{L}\,e^{j\omega_n t}\left(-\rho_{eff}{\omega_n}^2 + j\mathrm{b}\omega_n {k_n}^2 + \mathrm{E}_{eff}{k_n}^2\right)}\sin\left(\frac{k_n \mathrm{g}}{2}\right)\cos\left(k_n \mathrm{d}\right)$$

$$k_n = \frac{n\,\pi}{L}$$

Keeping other variables constant, V_{piezo} is maximum when $\cos(k_n d)$ is ±1 i.e. when, for an integer m:

$$2\frac{n\,\pi}{L}d = m\,\pi$$

$$\frac{2\,n}{L}d = m$$

As $L = 2\,d + g + 2\,L_{Mo}$, we can see why a higher harmonic, n, gives us more values of m for which $\cos^2(k_n d)$ is maximized, giving us a higher V_{piezo}, higher i_{out} and lower R_X.

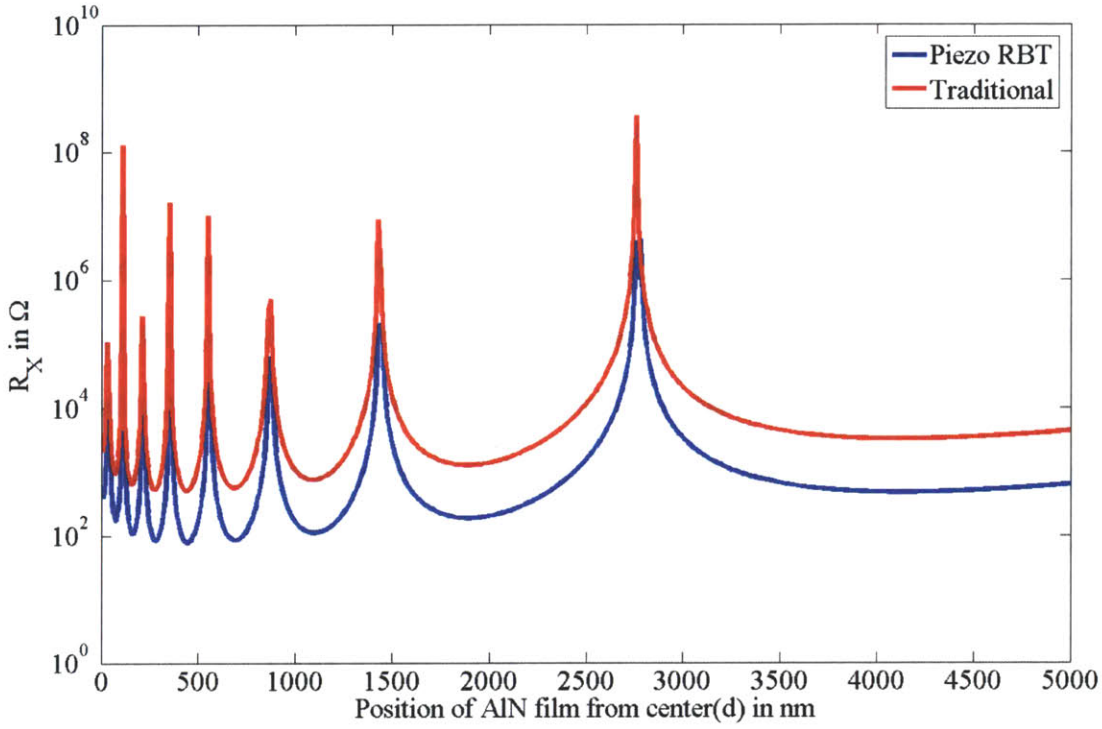

Figure 3.14: Plot of R_X as a function of the position of the piezoelectric films from the center of the device (d) for device operating in the ninth harmonic $n = 9$ for piezoelectric RBT and traditional piezoelectric resonator having a 100 nm AlN film and operating at 5 GHz.

Next, we consider optimizing the AlN film thickness towards the goal or decreasing the R_X as shown in Figure [3.15]. Similar to the previous optimization for film position, from an application perspective, we hold the frequency constant at 5 GHz while changing the thickness of the film. We once again observe the same periodicity in the R_X with film thickness as observed and explained before as the voltage V_{piezo} is a sinusoidal function of the film thickness g as well. For all thicknesses, the Piezoelectric RBT has approximately an order of magnitude lower R_X than the traditional resonator. From this plot, we may also infer that the AlN film thickness should be as small as possible in order to obtain the minimum possible motional impedance.

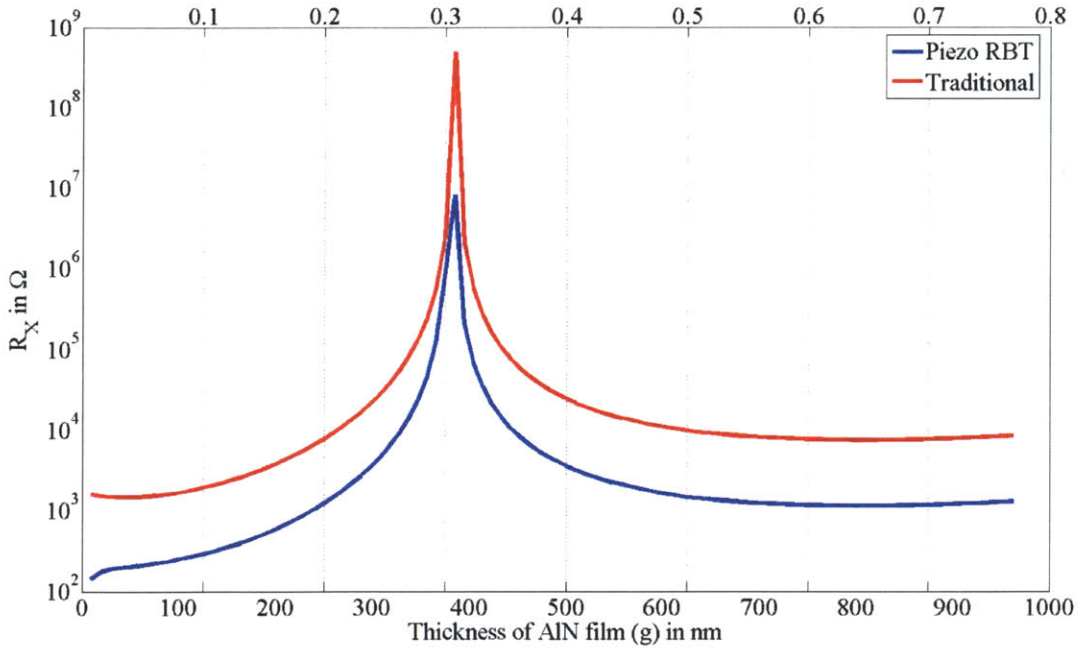

Figure 3.15: Plot of R_X as a function of the thickness of the piezoelectric films (g) normalized to the wavelength as shown on scale at top (λ) for device operating in the third harmonic $n = 3$ at a frequency of 5 GHz for piezoelectric RBT and traditional piezoelectric resonator.

So far, we have seen that the Piezoelectric RBT outperforms the traditional piezoelectric resonator in terms of motional impedance. We note though, that the width of the traditional piezoelectric resonator has been set to 2 μm more than L_{gate} to account for the source and drain regions while keeping the total size of the resonators the same. The length of the gate might be a parameter which suggests a possible tradeoff point between the two designs. We thus plot the R_X values vs the gate length, L_{gate} [Figure 3.16] and observe that such a tradeoff does exist. This may be explained by the fact that increasing the gate length reduces the transistor DC current. Hence the AC output current i_{out} drops and the R_X increases. On the other hand, increasing L_{gate} causes an increase in the effective sensing area of the traditional resonator, thus lowering its R_X.

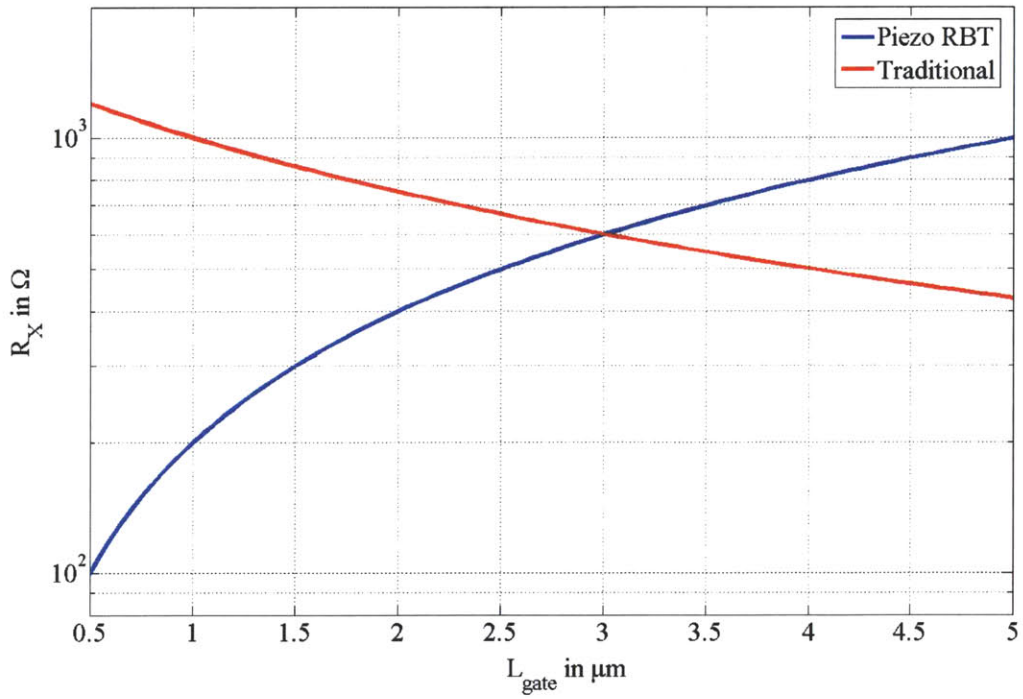

Figure 3.16: Plot of R_X as a function of the gate length (L_{gate}) for width $W = L_{gate} + 2\ \mu m$ for piezoelectric RBT and traditional piezoelectric resonator operating in the third harmonic $n = 3$

We now plot the tradeoff of using the Piezoelectric RBT vs the Traditional Piezoelectric Resonator over a range of frequencies. Keeping the commercially available AlN film fabrication techniques in mind, we plot this for a device operating at the third harmonic with a 50 nm AlN film, optimizing the Rx for the film position between 30 nm and 4 um from the center of the device [Figure 3.17]. We notice that the traditional piezoelectric resonator has a lower impedance at frequencies higher than 35 GHz.

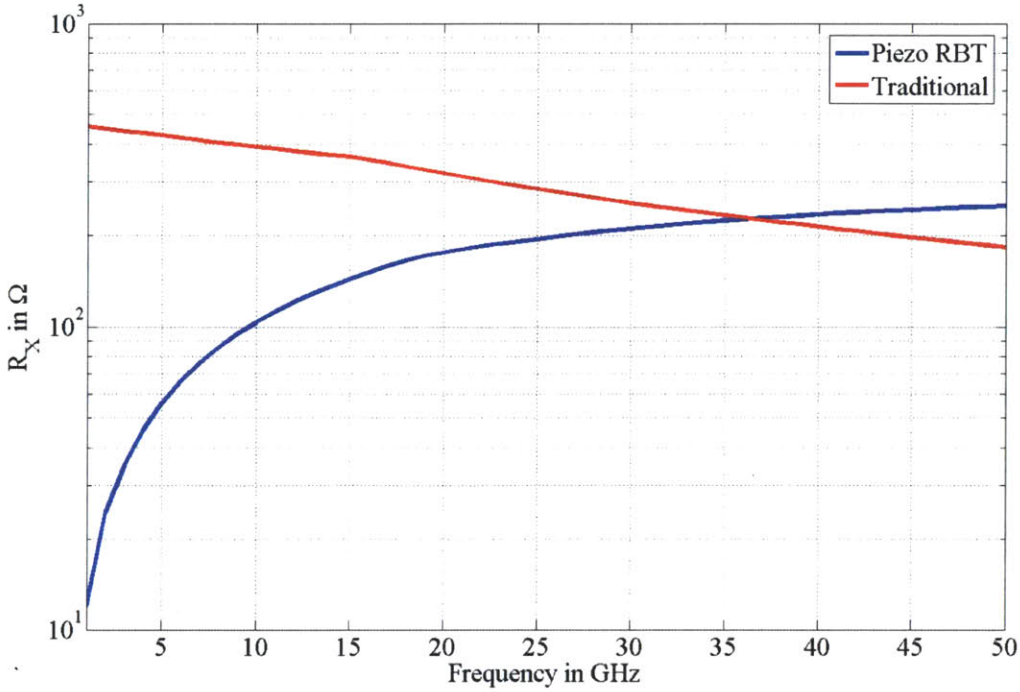

Figure 3.17: Plot of R_X as a function of the frequency for piezoelectric RBT and traditional piezoelectric resonator operating in the third harmonic $n = 3$ and 50 nm thick AlN films.

CONCLUSION

Combining the advantages of the high quality factors of Silicon based resonators and the high transduction efficiency of piezoelectric films, the Piezoelectric Resonant Body Transistor offers a low impedance, small footprint component that may be integrated into GHz-frequency transceiver circuitry as a low impedance high-Q component. A full analytical model of the Piezoelectric RBT as well as its traditional piezoelectric resonator counterpart has been presented in this work. The tradeoffs for choosing one design versus the other have been extensively discussed based on the fabrication possibilities and intended applications.

While analyzing the above trends, the inherent assumptions are that the film quality remains the same and that the piezoelectric coefficients and electrical characteristics of the film do not change with thickness, substrate (Silicon) orientation etc. Thus, the future work includes a first-run fabrication and characterization of the AlN film quality which may then be included in the device model and used to fabricate a prototype device.

BIBLIOGRAPHY

1. Nathanson, H.C.; Newell, W.E.; Wickstrom, R.A.; Davis, J.R., Jr.; , "The resonant gate transistor," *IEEE Transactions on Electron Devices* , vol.14, no.3, pp. 117- 133, (1967)

2. W. C. Tang, T.-C. H. Nguyen, M. W. Judy, and R. T. Howe, "Electrostatic-Comb Drive of Lateral Polysilicon Resonators," *Sensors and Actuators A*, A21-A23, 328-331, (1990)

3. Tang, W.C.; Lim, M.G.; Howe, R.T.; , "Electrostatically balanced comb drive for controlled levitation," *Solid-State Sensor and Actuator Workshop, 1990. 4th Technical Digest., IEEE* , vol., no., pp.23-27, 4-7 Jun 1990

4. Bhave, S.A.; Howe, R.T.; , "Silicon nitride-on-silicon bar resonator using internal electrostatic transduction," *Solid-State Sensors, Actuators and Microsystems, 2005. Digest of Technical Papers. The 13th International Conference on TRANSDUCERS '05.*, vol.2, pp. 2139- 2142, 5-9 June 2005

5. Weinstein, D.; Bhave, S.A.; , "Internal Dielectric Transduction of a 4.5 GHz Silicon Bar Resonator", *IEEE International Electron Devices Meeting (IEDM 2007)*, Washington, DC, December 10-12, 2007, pp. 415-418.

6. Weinstein, D.; Bhave, S.A.; , "The Resonant Body Transistor," *Nano Letters* 10(4) 1234-37 (2010).

7. G. Piazza. "Piezoelectric Aluminum Nitride Vibrating RF MEMS for Radio Front-End Technology," PhD Thesis, University of California, Berkeley, Dec 2005

8. P. J. Stephanou. "Piezoelectric Aluminum Nitride MEMS Resonators for RF Signal Processing," PhD Thesis, University of California, Berkeley, Dec 2006

9. Hung, Li-Wen; Nguyen, Clark T.-C.; , "Capacitive-piezoelectric AlN resonators with Q>12,000," *IEEE 24th International Conference on Micro Electro Mechanical Systems,* pp.173-176, 23-27 Jan. 2011

10. Abdolvand, R.; Ayazi, F.; , "Enhanced Power Handling and Quality Factor in Thin-Film Piezoelectric-on-Substrate Resonators," *IEEE Ultrasonics Symposium,* pp.608-611, 28-31 Oct. 2007

11. Samarao, A.K.; Ayazi, F.; , "Combined capacitive and piezoelectric transduction for high performance silicon microresonators," *IEEE 24th International Conference on Micro Electro Mechanical Systems*, pp.169-172, 23-27 Jan. 2011

12. Wang, W.; Popa, L. C.; Marathe, R.; Weinstein, D.; , "An unreleased mm-wave Resonant Body Transistor," *IEEE 24th International Conference on Micro Electro Mechanical Systems*, pp.1341-1344, 23-27 Jan. 2011

13. R. Abdolvand and F. Ayazi, "Narrow-Band Monolithic Piezoelectric-on-Substrate Filter Technology," *Proc. IEEE MTT-S International Microwave Symposium*, Honolulu, Hawaii, June 2007, pp. 509-512.

14. C. Zuo, J. Van der Spiegel, G. Piazza, "Switch-Less Dual-Frequency Reconfigurable CMOS Oscillator Using One Single Piezoelectric AlN MEMS Resonator with Co-Existing S0 and S1 Lamb-Wave Modes", *IEEE International Conference on Micro Electro Mechanical Systems*, Cancun, Mexico, 23-27 January, pp. 177-180.

15. Kaajakari, V.; Alastalo, A.T.; Mattila, T.; , "Electrostatic transducers for micromechanical resonators: free space and solid dielectric," *IEEE Transactions on Ultrasonics, Ferroelectrics and Frequency Control*, vol.53, no.12, pp.2484-2489, December 2006

16. Greeneich, E. W.; Muller, R. S.; , "Theoretical transducer properties of piezoelectric insulator FET transducers," *Journal of Applied Physics* , vol.46, no.11, pp.4631-4640, Nov 1975

17. Del Alamo, J. A., "Integrated Microelectronic Devices: Physics and Modeling," Prentice Hall, 2010

18. Kanda, Y. , "A graphical representation of the piezoresistance coefficients in silicon," *IEEE Transactions on Electron Devices,* vol.29, no.1, pp. 64- 70, Jan 1982

19. Yimnirun, R.; Eury, S.M.-L.; Sundar, V.; Moses, P.J.; Sei-Joo Jang; Newnham, R.E.; , "Electrostriction measurements on low permittivity dielectrics," Annual Report. *Conference on Electrical Insulation and Dielectric Phenomena*, pp.240-243, 25-28 Oct 1998

20. D. Weinstein, "The Resonant Body Transistor," PhD Thesis, Cornell University, Aug 2009

21. R. Tabrizian, M. Rais-Zadeh, F. Ayazi;, "Effect of phonon interactions on limiting the f.Q product of micromechanical resonators," *Proc. of IEEE Transducers*, 2131-34 (2009)

22. Stevens, K. S.; Ohtani, A.; Kinniburgh, M.; Beresford, R.; , "Microstructure of AlN on Si (111) grown by plasma-assisted molecular beam epitaxy," *Applied Physics Letters* , vol.65, no.3, pp.321-323, Jul 1994

23. Larson, J.D., III; Ruby, R.; Bradley, P.; Oshmyansky, Y.; , "A BAW antenna duplexer for the 1900 MHz PCS band," *Ultrasonics Symposium, 1999. Proceedings. 1999 IEEE* , vol.2, no., pp.887-890 vol.2, 1999